



Cite this: *Nanoscale Adv.*, 2025, 7, 2483

High specific surface area MMT/NO₂ intercalated modified MgAl-LDH core–shell composites: effective inhibition for steel in Cl[−] contaminated saturated Ca(OH)₂ solution

Xiaoyi Zhang,^{ab} Binxin Gan,^a Chen Wu,^{ab} Guoliang Lin,^a Shenglan Ma,^a Yongbin Ye,^c Wanxi Jiang^d and Wenjin Huang^e

This study developed nitrate-intercalated layered double hydroxides (NO₂-LDHs) and their core–shell composites (NO₂-LDHs@MMT) through an *in situ* co-precipitation method with montmorillonite (MMT). The corrosion inhibition performance for Q235 steel in simulated concrete pore solutions (saturated Ca(OH)₂ + 3.5 wt% NaCl) was systematically investigated. Comprehensive characterization via scanning electron microscopy (SEM), energy-dispersive spectroscopy (EDS), high-resolution transmission electron microscopy (HRTEM), X-ray diffraction (XRD), X-ray photoelectron spectroscopy (XPS), and Fourier-transform infrared spectroscopy (FTIR) confirmed the successful construction of core–shell architecture and effective intercalation of nitrite anions between LDH layers. Nitrogen physisorption analysis revealed that the NO₂-LDHs@MMT composite possesses a specific surface area of 84.74 m² g^{−1} with a pore volume of 0.284 cm³ g^{−1}, forming a hierarchical pore structure conducive to chloride ion entrapment. Electrochemical assessments including electrochemical impedance spectroscopy (EIS) and potentiodynamic polarization demonstrated that both materials significantly improved the corrosion resistance of steel substrates, with NO₂-LDHs@MMT exhibiting superior performance (98.9% inhibition efficiency). The enhanced anticorrosion mechanism originates from: (1) the MMT core providing enlarged surface area for LDH growth, increasing active sites for Cl[−] adsorption; (2) sustained release of NO₂[−] from LDH galleries enabling stable passivation layer formation. These findings suggest that NO₂-LDHs@MMT composites hold promise as high-efficiency, durable corrosion inhibitors for steel reinforcement in chloride-contaminated alkaline environments.

Received 4th December 2024
Accepted 26th February 2025

DOI: 10.1039/d4na01011f
rsc.li/nanoscale-advances

1. Introduction

In recent years, with the rapid development of marine engineering, the durability and recovery capabilities of marine concrete structures have become critical concerns for researchers and engineers alike.^{1–3} Chloride-induced steel reinforcement corrosion is one of the most critical factors compromising the durability of marine concrete structures. Chloride ions, which are ubiquitous in marine environments, can penetrate concrete and reach the surface of steel reinforcement, triggering corrosion. This not only compromises the structural performance of the concrete but also significantly

shortens its service life.^{4–6} Therefore, comprehensively understanding the impact of chloride-induced steel corrosion on marine concrete and exploring effective corrosion prevention measures are essential for ensuring the safety and longevity of marine concrete structures.⁷

Layered double hydroxides (LDHs) are a unique class of layered compounds with the general formula [M²⁺_{1-x}M³⁺_x(OH)₂(x + 1)(A^{n−})_{x/n}·yH₂O], where M²⁺ and M³⁺ represent divalent and trivalent metal cations, respectively, and A^{n−} denotes interlayer anions.^{8–10} LDHs exhibit excellent interlayer anion exchange properties, making them ideal candidates for adsorbing and storing corrosive anions such as chloride ions (Cl[−]) in cement-based materials. Additionally, the hydration products of cement, such as AFm phases, belong to the family of calcium–aluminum hydroxyl-like compounds (Ca-LDHs), highlighting the potential of LDHs to enhance the properties of cementitious materials.¹¹ In recent years, the extensive applications of intercalated Layered Double Hydroxide (LDH) materials in energy storage, catalytic conversion^{12,13} and other fields

^aFujian Key Laboratory of New Technology and Information Technology in Civil Engineering, Fujian University of Technology, Fuzhou, 350118, China. E-mail: xy-zhang@fjut.edu.cn; Fax: +86-591-22863252; Tel: +86-591-22863252

^bFujian Key Laboratory of Digital Simulations for Coastal Civil Engineering, School of Architecture and Civil Engineering, Xiamen University, Xiamen, 361005, China

^cFujian Xingyan Construction Group Co., Ltd, China

^dCNNC Huachen Engineering Management Co., Ltd, China

^eXiamen Special Economic Zone Construction and Investment Group Co., Ltd, China



have further validated the universality of their functional design.

Existing studies have shown that LDHs significantly improve the early strength of concrete and enhance its durability against chloride penetration and carbonation.^{14–16} For instance, Tate-matsu *et al.*¹⁷ incorporated nitrate-intercalated LDHs into mortar to repair chloride-induced corrosion in reinforced concrete, observing a notable increase in electrode potential and a substantial reduction in free chloride ions within the mortar. Similarly, Shui *et al.*¹⁸ demonstrated that LDHs effectively increased the chloride adsorption capacity of cement paste, delaying the ingress of chloride ions into concrete structures. Xu *et al.*^{19,20} synthesized nitrate-intercalated LDHs *via* co-precipitation, achieving outstanding chloride adsorption performance and corrosion inhibition in simulated concrete pore solutions. Zhou *et al.*²¹ incorporated nano-SiO₂ into nitrate-intercalated LDHs, significantly enhancing the chloride adsorption capacity and corrosion inhibition effectiveness of the resulting composites.

However, traditional LDHs face several limitations, such as hydrophilicity and high surface charge density, which lead to the aggregation of plate-like particles and hinder their dispersion and practical application.²² Additionally, traditional LDHs exhibit relatively low specific surface areas and lack precise control over crystal morphology and particle size distribution, often forming irregular large particles. These factors limit the accessibility of interlayer channels for anions, thereby reducing their adsorption and exchange capacities.^{23–25} To address these challenges, one promising strategy involves growing LDH nanosheets on nanoparticle substrates to form core–shell composite materials.²⁶ Design strategies^{27–29} involving such core–shell structures have optimized material stability and active site exposure efficiency through interface engineering.

In recent years, researchers have proposed the use of inorganic substrates, such as zeolites, SiO₂, and montmorillonite (MMT), as templates for the vertical growth of LDH nanosheets. For example, Chen *et al.*^{30,31} synthesized LDH nanosheets on the surfaces of zeolites and SiO₂, significantly increasing the specific surface area and demonstrating enhanced chloride adsorption efficiency. Ke *et al.*³² showed that Mg–Al and Ca–Al LDHs effectively adsorbed chloride ions under high-alkalinity conditions, with uniformly distributed adsorption sites. Li *et al.*³³ further advanced the development of core–shell composite materials, achieving significantly improved hydrophobicity and adsorption capacities.

Building upon these advancements, this study developed a novel nitrate-intercalated magnesium–aluminum layered double hydroxide@montmorillonite (MgAl-LDHs@MMT) core–shell composite material. By optimizing the MMT content, the specific surface area and stability of the composite material were significantly enhanced. The performance of this composite in chloride adsorption and corrosion inhibition of steel reinforcement was evaluated in simulated concrete pore solutions. Various characterization techniques, including X-ray diffraction (XRD), Fourier-transform infrared spectroscopy (FTIR), and scanning electron microscopy-energy dispersive X-ray spectroscopy (SEM-EDS), were employed to investigate the

adsorption mechanism and corrosion inhibition properties. The study also validated the dynamic adsorption–release properties and long-term durability of NO₂-LDHs@MMT in high-salinity and humid environments.

The MMT material used in this study is abundant, cost-effective, and environmentally friendly, and the synthesis process aligns with the principles of green chemistry, making it suitable for industrial-scale production. These attributes provide NO₂-LDHs@MMT with significant economic advantages and practicality for large-scale engineering applications.

2. Materials and methods

2.1. Raw materials

The raw materials, namely Mg(NO₃)₂·6H₂O, Al(NO₃)₃·9H₂O, NaNO₂, Ca(OH)₂, NaCl, and NaOH, were procured from Sino-pharm Chemical Reagent Co., Ltd. Na-MMT (K-10) was purchased from Macklin Biochemical Co., Ltd. All chemical reagents were of analytical purity, and all solutions employed in the experiment were prepared with deionised water to eliminate the potential influence of other impurity ions.

2.2. Preparation of NO₂-intercalated MgAl-LDHs and MgAl-NO₂-LDHs modified with MMT

In this study, NO₂-LDHs@MMT composites were prepared *via* the *in situ* co-precipitation method. During the synthesis process, the pH of the system was adjusted and maintained at approximately 10 through the dropwise addition of NaOH. The temperature was maintained at 80 °C, and the precipitation time was 2 h. Subsequently, the composites were aged for 24 h at room temperature. The selection of pH = 10 was predicated under the optimal conditions for the formation of the LDH laminate structure, which also ensures the activation of functional groups on the MMT surface and facilitates the formation of the composite structure.³⁴ The specific experimental procedure was as follows: 50 mL of a mixed solution of Al(NO₃)₃·9H₂O (46.89 g, 0.125 mol) and Mg(NO₃)₂·6H₂O (96.15 g, 0.375 mol) was added slowly to a three-necked flask containing 30 mL of deionised water. Concurrently, a solution of NaOH (40 g, 1 mol) and NaNO₂ (138 g, 2 mol) was added dropwise under vigorous stirring, and the rate of addition was adjusted to maintain a pH of 9–10. Once the addition was complete, the mixed solution was stirred at 80 °C for 24 h. The mixed solution was centrifuged and filtered to obtain white crystals. These crystals were repeatedly washed with deionised water and anhydrous ethanol until neutral, then dried, ground, and sieved through a 400-mesh sieve. The NO₂-LDHs@MMT material can be obtained by replacing the deionised water in the synthesis of NO₂-LDHs with a mixed solution doped with 0.3 g Na-MMT (K-10) after standing for 24 h. For further details on the synthesis of NO₂-LDHs, please refer to the relevant literature.³⁵

2.3. Microstructure measurements

The surface morphologies of the synthesized NO₂-LDHs and NO₂-LDHs@MMT were meticulously examined using a scanning electron microscope (ZEISS Gemini SEM 300). The specific

surface areas of both NO_2 -LDHs and NO_2 -LDHs@MMT were determined through N_2 adsorption–desorption experiments conducted on an automated surface area analyzer (ASAP 2020). These surface areas were subsequently calculated employing the Brunauer–Emmett–Teller (BET) equation. Prior to BET analysis, the samples underwent a rigorous degassing process at 100 °C for a minimum duration of 10 h to eliminate any adsorbed gases or impurities. To characterize the crystalline structures of the LDH samples, an X-ray diffractometer (Rigaku SmartLab SE) equipped with $\text{Cu K}\alpha$ radiation ($\lambda = 0.1541844$ nm) operating at 40 kV and 40 mA was employed. To determine the detailed characteristics of the structure, high-resolution transmission electron microscopy (HRTEM) (JEM-2100) was performed at an accelerating voltage of 200 kV. The surface elemental analysis was performed using an (ESCALAB Xi+) X-ray photoelectron spectroscope (XPS) equipped with a monochromated Al-K X-ray source (1486.6 eV) at a pass energy of 40 eV. The diffraction patterns were recorded at a scan rate of 2° min⁻¹, spanning a diffraction angle range of 5–90°, providing detailed insights into the crystallinity of the LDH materials. Additionally, the functional groups and chemical bonding within the LDH samples were investigated through Fourier transform infrared (FT-IR) spectroscopy, utilizing a Thermo Scientific Nicolet iS20 analyzer. The FT-IR spectra were acquired within a wavelength range of 4000–400 cm⁻¹, adopting the KBr pellet method for sample preparation. Furthermore, the thermal stability and decomposition behavior of the LDH samples were assessed using a Netzsch STA 449 F3 thermogravimetric analyzer. The TG tests were conducted under a nitrogen atmosphere, with a heating rate of 10 °C min⁻¹, within a temperature range of 30–800 °C. The researchers employed a multifaceted approach, including SEM imaging, TEM imaging, XPS spectrum, BET surface area measurements, XRD crystallography, FTIR spectroscopy, and TG-DTG thermal analysis, to provide a comprehensive characterization of the synthesized NO_2 -LDHs and NO_2 -LDHs@MMT materials.

2.4. Equilibrium isotherm of chloride ions

In order to investigate the chloride ion adsorption capabilities of 1 g of NO_2 -LDHs or NO_2 -LDHs@MMT, these materials were introduced individually into 100 mL of saturated $\text{Ca}(\text{OH})_2$ solutions. The solutions contained varying concentrations of NaCl , ranging from 10 to 400 mmol L⁻¹, with intervals of 10, 20, 40, 60, 80, 100, and 200 mmol L⁻¹. The resulting mixtures were transferred to 250 mL conical flasks and agitated continuously for 24 h at 25 °C to allow for adsorption to occur. The chloride ion concentration was determined using the chloride ion selective electrode method, whereby the E (mV) value and the corresponding $\log[\text{C}(\text{Cl}^-)]$ value were established by measuring standard solutions of chloride ions with varying concentrations. This process enabled the establishment of a correlation between the potential value and the chloride ion concentration using a PCL-1-01 model. The potential E (mV) was determined using a DZS-706F multi-parameter analyser, employing a chlorine ion-selective electrode and a $\text{C}(\text{K}_2\text{SO}_4)$ reference electrode. Subsequently, the chlorine ion concentration of the tested

sample was calculated from the standard curve. It is advised that the electrode be rinsed with deionised water prior to measurement. The chloride ion adsorption capacity (q_e , mg g⁻¹) of NO_2 -LDHs@MMT or NO_2 -LDHs was calculated using eqn (1):

$$q_e = \frac{(C_0 - C_e)V}{m} \quad (1)$$

where m is the mass of NO_2 -LDHs@MMT or NO_2 -LDHs added (g). The initial concentration of chloride ions (mg L⁻¹) is represented by C_0 . V represents the volume of saturated calcium hydroxide solution (L).

2.5. Chloride penetration and corrosion monitoring

In order to facilitate a comparison of the corrosion inhibition properties of NO_2 -LDHs@MMT and NO_2 -LDHs for steel reinforcement, tests were conducted on a CHI760E electrochemical workstation. The test system was based on a three-electrode configuration, with the saturated calomel electrode (SCE) serving as the reference electrode and the counter electrode comprising a platinum electrode. The steel bars utilized in the experiment were HPB235, with a chemical composition of 0.15 wt% C, 0.17 wt% Si, 0.38 wt% Mn, 0.01 wt% S, 0.09 wt% P, and residual Fe. A Q235 carbon steel specimen with an exposed surface area of 0.785 cm² was employed as the working electrode, with dimensions of 10 mm in diameter and 10 mm in length. The working surface was the one end face of the steel rod, which was connected to a copper wire at the other end. All surfaces of the steel rod, with the exception of the working surface, were sealed with epoxy resin, forming a protective coating. Prior to the commencement of the experiment, the steel rods were sanded with 150–2000 grit sandpaper, and then cleaned with acetone and deionised water. The test solution was a saturated calcium hydroxide solution containing 3.5 wt% sodium chloride, dispersed with 1 g L⁻¹ nitrilotriacetic acid-functionalized layered double hydroxide@montmorillonite or nitrilotriacetic acid. Electrochemical impedance spectroscopy (EIS) tests were conducted at open-circuit potentials (OCPs) and with sinusoidal AC signals with an amplitude of 10 mV, spanning a frequency range from 0.01 Hz to 100 kHz. The specimens were immersed in the solution for varying durations: 6, 12, 24, 36, 48, 60 and 72 h. Polarisation tests were conducted after 72 h, while the Tafel polarisation method was tested with the scanning range set to open circuit potential ± 300 mV, scanning speed of 1 mV s⁻¹ and room temperature as the experimental temperature.

3. Results and discussion

3.1. Determination of the optimal dosage of MMT in NO_2 -LDHs@MMT composites

Fig. 1 depicts a schematic representation of the strategy employed for the synthesis of LDHs. The objective of the synthetic work was to successfully intercalate NO_2^- between the layered double hydroxides, thereby enabling chloride exchange and adsorption. MMT is employed as a template for the modification of NO_2 -LDH composites; however, the dosage of the template directly influences the adsorption properties of the

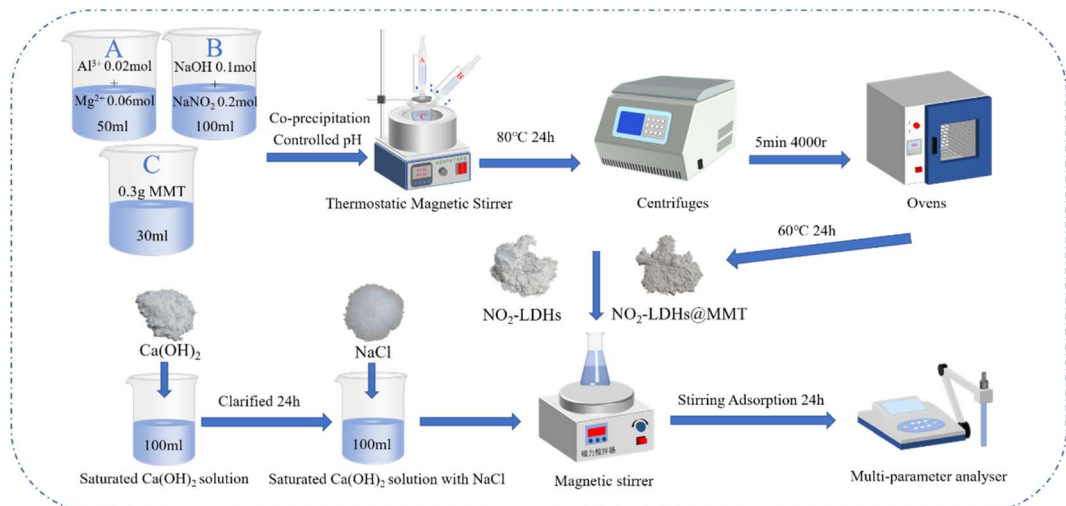


Fig. 1 (A) Flow chart for the preparation of NO_2 -LDHs and (B and C) experimental set up of the simulated solutions.

resulting NO_2 -LDHs@MMT composites. Ten MMT mass ratios ranging from 2 wt% to 20 wt% with 2 wt% increments were designed for synthesizing the NO_2 -LDHs@MMT composite materials. Comparative tests were conducted on the adsorption properties of chloride (Cl^-) in a 100 mmol L^{-1} Cl^- solution for the synthesised NO_2 -LDHs@MMT with varying MMT doping ratios. The optimal MMT doping ratio was selected, and the resulting adsorption curves are presented in Fig. 2. As the MMT doping ratio increased, the adsorption capacity of the NO_2 -LDHs@MMT composite exhibited an initial upward trend, followed by a decline. The optimal adsorption capacity of the NO_2 -LDHs@MMT composite was attained at a doping ratio of 6 wt%. Research indicated that an appropriate MMT content could effectively enhance the loading capacity of NO_2 -LDHs, increase the specific surface area, and ensure optimal dispersion, resulting in the uniform distribution of NO_2 -LDHs between MMT layers. This improved the surface affinity of the composite material, facilitating better interaction with target substances in

practical applications. However, excessive MMT could adsorb an excessive amount of metal ions from the precursors, altering the $\text{Mg}^{2+}/\text{Al}^{3+}$ molar ratio in the LDH composites. This led to excessive surface coverage, structural agglomeration, and non-uniform distribution, negatively impacting the stability, performance, and reactivity of the NO_2 -LDHs@MMT, thus reducing the material's chloride ion adsorption capacity.^{36,37}

3.2. Characterization of synthesized NO_2 -LDHs and NO_2 -LDHs@MMT

3.2.1. XRD and FTIR. Fig. 3 illustrates the XRD patterns of MMT, NO_2 -LDHs and NO_2 -LDHs@MMT before and after 2 h of adsorption in simulated concrete pore solutions. In comparison with the standard material card JCPDS 99-000-1633 for MgAl-LDHs, the two materials, NO_2 -LDHs and NO_2 -LDHs@MMT, exhibited distinct diffraction peaks that aligned with the series of crystal planes of hydrotalcite, both before and after the

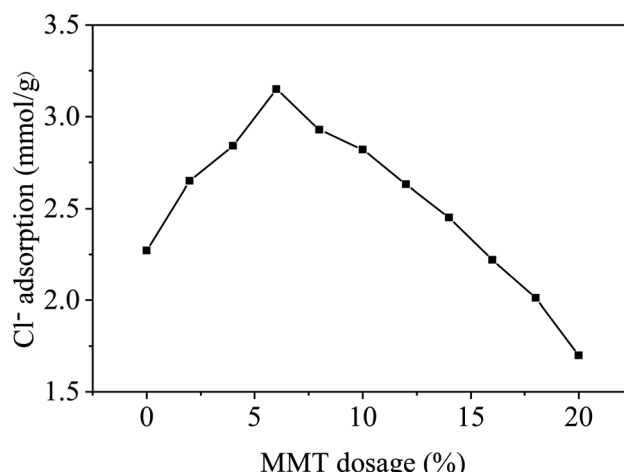


Fig. 2 Adsorption of Cl^- in 100 mmol L^{-1} Cl^- solution by the synthesised NO_2 -LDHs@MMT with different MMT doping levels.

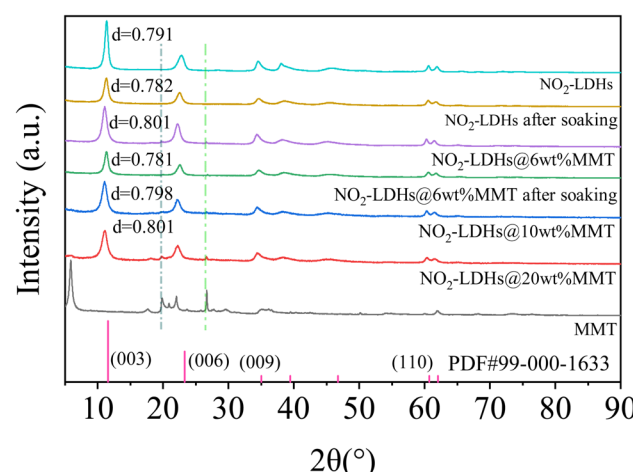


Fig. 3 XRD patterns of MMT, NO_2 -LDHs and NO_2 -LDHs@MMT before and after 2 h adsorption in simulated concrete pore solutions.



adsorption of chloride ions had taken place. The diffraction peaks observed in the XRD patterns of the NO_2 -LDHs@MMT samples were found to correspond to those of hydrotalcite, both prior to and following the adsorption of chloride ions. The aforementioned peaks were found to correspond to the (003), (006), (009), and (110) crystal planes of hydrotalcite, respectively. This indicated that the LDHs retained a robust crystalline structure and crystallinity following their growth on MMT. The diffraction peaks of the NO_2 -LDHs@MMT crystal planes were not discernible in the presence of the MMT material. This can be attributed to the fact that the mass of the MMT was significantly less than that of the LDHs grown on it, which rendered it undetectable. This finding was in accordance with the results of the SEM image observations that had been made. However, following the adsorption of chloride ions, a decrease in the intensity of the characteristic peaks was observed, accompanied by a shift of the diffraction peaks on the (003) crystal plane to the right and a reduction in the layer spacing. A shift in 2θ was observed in the NO_2 -LDHs from 11.18° to 11.30° , accompanied by a decrease in layer spacing from 0.791 nm to 0.782 nm. Similarly, NO_2 -LDHs@MMT exhibited a shift in 2θ from 11.04° to 11.32° , accompanied by a decrease in layer spacing from 0.801 nm to 0.781 nm. The replacement of the NO_2^- and NO_3^- ions with chloride ions, which have a smaller ionic radius, resulted in a decrease in the layer spacing. Both NO_2 -LDHs and NO_2 -LDHs@MMT exhibited identical adsorption trends for chloride ions, suggesting a shared adsorption mechanism. This finding aligns with previous studies.^{17,31}

Fig. 4 illustrates the infrared spectra of MMT, NO_2 -LDHs, and NO_2 -LDHs@MMT, both prior to and following the adsorption of chloride ions. The broad peak observed near 3470 cm^{-1} was attributed to the stretching and vibration of O-H in the crystal water of the LDH layer. The observed phenomena indicated that LDHs had adsorbed or intercalated a considerable number of water molecules between the layers and on the surface. The infrared peak at approximately 1637 cm^{-1} was attributed to the bending vibration of the bound hydroxyl group ($-\text{OH}$) on the LDH layer. In the case of MMT, an absorption peak

is observed as a result of Si-O stretching and bending vibrations, occurring at a wavelength of approximately 1034 cm^{-1} . Similarly, an absorption peak was observed in NO_2 -LDHs@MMT and the Si-O peaks continue to increase with increasing MMT doping in the LDHs. This indicates that LDHs have formed a composite material with MMT. Prior to the adsorption of chloride ions, the stretching vibration peaks corresponding to NO_3^- and NO_2^- were observed at 1383 cm^{-1} and 1265 cm^{-1} , respectively. The ratio of peaks corresponding to NO_2^- to peaks corresponding to NO_3^- changed from NO_2 -LDH samples to NO_2 -LDHs@MMT samples. This is caused by the difference in the content or chemical environment of the NO_2^- and NO_3^- peaks in NO_2 -LDHs and NO_2 -LDHs@MMT. Following the adsorption of chloride ions, a notable decline was observed in the stretching vibration peaks of NO_3^- and NO_2^- . In particular, the NO_2^- peak became undetectable. This indicated that NO_2 -LDHs and NO_2 -LDHs@MMT facilitated the release of NO_3^- and NO_2^- between the LDH layers, thereby achieving electrical neutrality. This finding was in accordance with the observations made in the XRD spectrum.

3.2.2. SEM-EDS and TEM. The SEM images of MMT, NO_2 -LDHs and NO_2 -LDHs@MMT are shown in Fig. 5, and EDS results are shown in Table 1. Both MMT and NO_2 -LDH samples exhibit the expected sheet morphology, with the sheets appearing to be tightly stacked (see Fig. 5a and b). In contrast, the NO_2 -LDHs@MMT samples exhibit a typical daisy-like morphology. It was clear that the LDH sheets were no longer stacked on top of each other, but instead grow vertically interleaved on the MMT surface, as shown in Fig. 5c and d. This observation may be due to the fact that the structural core of the MMT provides three-dimensional spatial orientation, allowing the LDHs to arrange in a layered manner (as opposed to a unidirectional stacking). This indicated that MMT and LDHs have been successfully combined to form a biomimetic core-shell structure similar to a sunflower. EDS analysis showed that NO_2 -LDHs@MMT contained N, O, Mg, Al and Si. Notably, the atomic percentage ratio of Mg^{2+} and Al^{3+} was 3 : 1, which was consistent with the atomic percentages in the prepared LDHs. This finding was also consistent with the conclusion that LDHs were successfully formed on the surface of MMT, as evidenced by the scanning electron microscope images. In contrast, the EDS data for Al^{3+} atoms in NO_2 -LDHs@MMT were greater than those for MMT and NO_2 -LDHs, which was due to the superposition of aluminium in MMT and LDHs. The combination of SEM images and XRD spectra revealed that MMT has a high specific surface area and a stable layered structure. This structure can be employed as a template to facilitate the vertical growth of LDH nanosheets, resulting in a more open three-dimensional structure (Fig. 5c). This structural property not only increases the specific surface area but also enhances the number of active sites of the material, thereby improving the adsorption performance of chloride ions. In conjunction with the FTIR patterns, it can be posited that the NO_2 -LDHs@MMT material exhibits a core-shell structure, with MMT constituting the core crystal. Nevertheless, since MMT only accounts for 6% of the total mass, the impact on the overall elemental composition of the NO_2 -LDHs@MMT was negligible. Energy

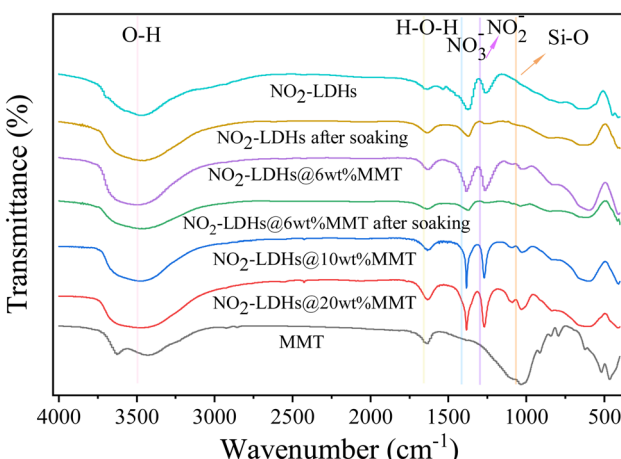


Fig. 4 FTIR patterns of MMT, NO_2 -LDHs and NO_2 -LDHs@MMT before and after 2 h adsorption in simulated concrete pore solutions.



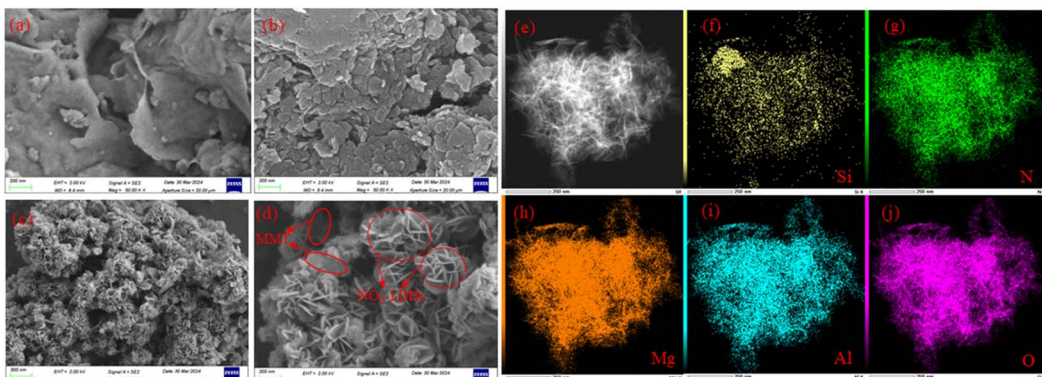


Fig. 5 SEM images of (a) MMT, (b) NO_2 -LDHs, (c and d) NO_2 -LDHs@MMT, (e–j) EDS mapping images of NO_2 -LDHs@MMT.

Table 1 EDS results of (a) MMT, (b) NO_2 -LDHs, (c and d) NO_2 -LDHs@MMT

Element (at%)	N	O	Mg	Al	Si
MMT	—	70.41	0.54	6.38	22.67
NO_2 -LDHs	4.82	72.72	16.65	5.81	—
NO_2 -LDHs@MMT	1.48	63.6	24.86	8.57	1.49

Dispersive Spectroscopy (EDS) mapping in Fig. 5(g and h) reveals the coexistence of elements O, Mg, Al, Si, and N in NO_2 -LDHs@MMT. MMT contributes elements such as Mg, Al, O, and Si, while LDHs provide elements such as O, Mg, Al, and N. Additionally, the EDS spectra indicate that Mg and Al are uniformly distributed on the MMT surface without significant separation, suggesting the successful growth of LDHs on the MMT surface.

Fig. 6 provides further insight into the intricate structural characteristics of ordinary NO_2 -LDHs and NO_2 -LDHs@MMT composites, prepared *via* the co-precipitation method, through the utilization of the TEM technique. As illustrated in Fig. 6a, the unmodified NO_2 -LDHs displayed a characteristic lamellar stacking morphology, which was in accordance with the observations made using SEM. By contrast, Fig. 6b and (c) illustrate the distinctive structure of NO_2 -LDHs@MMT, in which the LDH nanosheets were successfully deposited and firmly attached to the surface of the MMT nanoparticles, forming a highly open hierarchical structure. In this structure, the LDH nanosheets were vertically aligned on the MMT surface and extended outward, effectively avoiding stacking between the nanosheets. This increased the specific surface area and the number of active sites of the material.³⁸ In addition, 0.20 nm crystal spacing is attributed to the (012) crystal faces of NO_2 -LDHs@MMT, respectively, as shown in Fig. 6d. Upon further zooming in to the high-resolution mode (Fig. 6d), the lattice stripes of NO_2 -LDHs@MMT could be clearly observed, with a lattice spacing of 0.2 nm.³⁹ The graphical contours of the lattice stripes (Fig. 6e) also verified the basal spacing of NO_2 -LDHs @MMT. This observation was in accordance with the (006) crystal surface of the hydrotalcite structure, as evidenced by XRD analysis, which further corroborated the successful

complexation of LDHs on the MMT surface and its excellent crystallinity. To ascertain the veracity of the conclusions, a series of heuristic circles were resolved by means of a fast Fourier transform (FFT), which also corroborated the existence of disparate planes of NO_2 -LDHs@MMT (Fig. 6f). The fundamental spacing of NO_2 -LDHs@MMT was also corroborated through the inversing of the FFT (Fig. 6g) and the graphical representation of the local lattice stripe spacing following the inversing (Fig. 6h). Prior research has demonstrated that a synthesis temperature of 80 °C and pH = 10 represent the optimal conditions for the preparation of LDH composites, facilitating the formation of a stable laminate structure.⁴⁰ The identical conditions were employed in the present study to guarantee the high crystallinity and optimal structural properties of the materials (Fig. 6). The objective of the experimental conditions in this study is to further optimise the templating role of MMT and the vertical growth properties of LDHs in comparison to the preparation conditions of conventional LDH composites.

3.2.3. XPS. The XPS full and high-resolution spectra of NO_2 -LDHs and NO_2 -LDHs@MMT, both before and after the adsorption of chloride ions, revealed the chemical composition and adsorption mechanism of the materials. As illustrated in Fig. 7, the XPS full spectrum (Fig. 7a) demonstrates the presence of elements including Al, Mg, Si, and N, which corroborates the anticipated composition of the material.⁴¹ Following the adsorption of chloride ions, the appearance of elemental Cl provided confirmation of the successful adsorption process. The unique Si 2p characteristic peaks of NO_2 -LDHs@MMT in the Si 2p spectrum (Fig. 7b) demonstrated the successful complexation of LDHs with MMT. The results of the high resolution spectra of N 1s (Fig. 7d) showed that the N 1s peaks of NO_2 -LDHs and NO_2 -LDHs@MMT disappeared upon adsorption of chloride ions, while a new Cl 2p peak appeared (Fig. 7c). This directly proved that NO_3^- and NO_2^- in the interlayer of LDHs were ion-exchanged with chloride ions.⁴² It is noteworthy that the relative contents of NO_2^- and NO_3^- in NO_2 -LDHs@MMT (9.9% and 4.29%) were higher than those in NO_2 -LDHs (3.21% and 2.01%), indicating that NO_2 -LDHs@MMT possessed a stronger Cl^- exchange capacity, which predicted its superior rust inhibition performance. Furthermore, the fitted spectra of



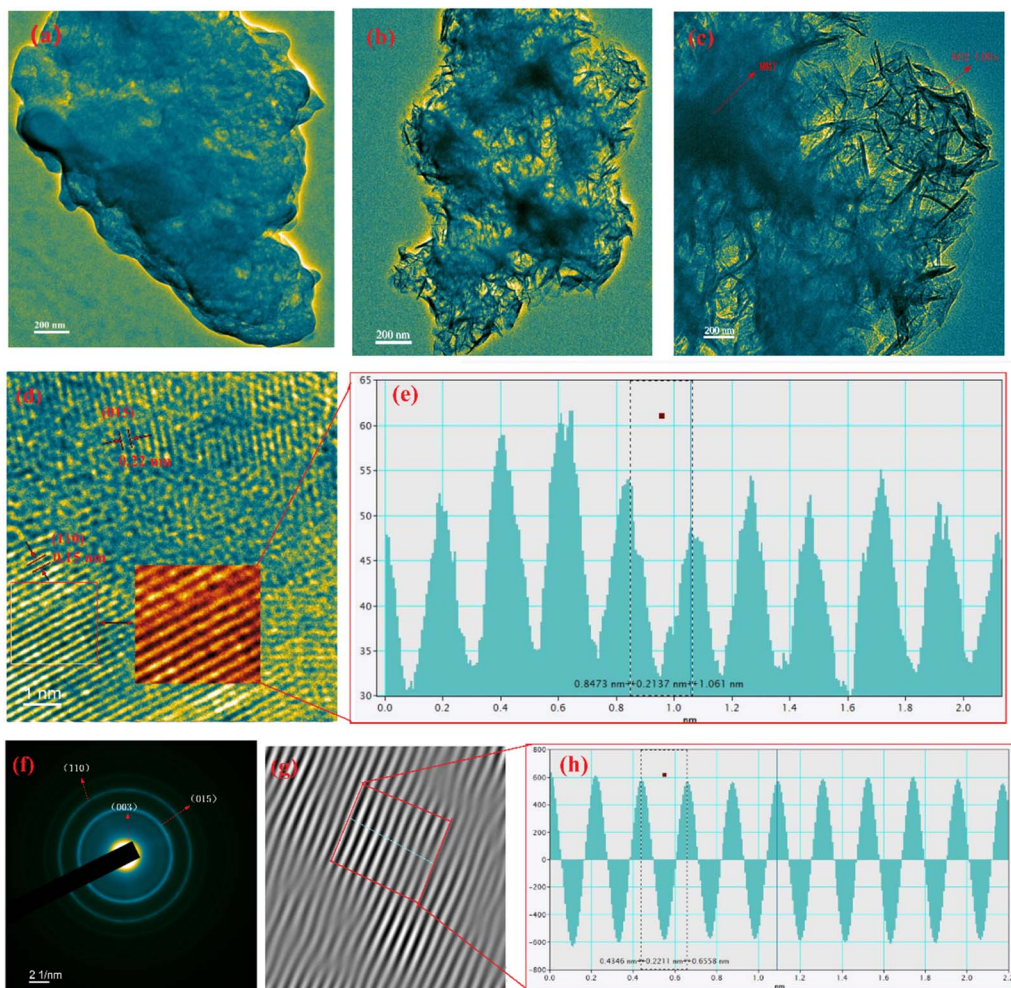


Fig. 6 (a) TEM images of NO_2 -LDHs; (b and c) TEM images of NO_2 -LDHs@MMT; (d) HRTEM image of NO_2 -LDHs@MMT; (e) plot profile of HRTEM lattice fringes of NO_2 -LDHs@MMT; (f) FFT pattern of NO_2 -LDHs@MMT; (g) IFFT pattern of NO_2 -LDHs@MMT; (h) plot profile of IFFT pattern lattice fringes of NO_2 -LDHs@MMT.

$\text{Mg}\ 1\text{s}$ (Fig. 7e) and $\text{Al}\ 2\text{p}$ (Fig. 7f) exhibited a shift in binding energy towards higher positions upon the adsorption of chloride ions. This was attributed to the redistribution of the electron cloud and the alteration in the energy level structure resulting from the strong electronegativity. The binding energies of $\text{Cl}\ 2\text{p}$ (199.4 eV and 197.8 eV) indicated that chloride ions were bound to the metal hydroxide laminates in the hydrogen bonding mode, which was stabilised in the interlayers, thus enhancing the corrosion resistance of the material.⁴³

3.2.4. TG-DTG and BET. The thermogravimetric curves (TG-DTG) delineated the four principal stages of decomposition observed in all synthetic samples, as well as the peaks of the derivative thermogravimetric analysis (DTG). The TG-DTG curves of the synthesised NO_2 -LDHs and NO_2 -LDHs@MMT are presented in Fig. 8. It was observed that LDHs exhibited a distinctive and characteristic thermal behaviour within the temperature range of 30 to 800 °C, with clearly identifiable stages of mass loss (see Fig. 8a and b). The TG curves indicated that the NO_2 -LDHs@MMT exhibited a lower degree of weight loss than the NO_2 -LDHs. Moreover, the thermal decompositon

pathways of both were characterised by three distinct steps. At temperatures below 200 °C, the water molecules adsorbed on the outer surface of NO_2 -LDHs@MMT and NO_2 -LDHs began to dehydrate and evaporate. This process corresponded to a relative weight loss of approximately 11.98% and 6.43%, respectively, as determined by TG analysis. The mass loss was primarily attributed to the elimination of crystal water and interlayer water, which had no impact on the layered structure of NO_2 -LDHs and NO_2 -LDHs@MMT. Subsequently, between 200 and 530 °C, the majority of the interlayer water in NO_2 -LDHs was eliminated, and the hydroxyl groups condensed between the layers (see Fig. 8a).

It was worthy of note that a comparable phenomenon was observed in NO_2 -LDHs@MMT within the temperature range of 200 to 430 °C (see Fig. 8b). This phenomenon can be attributed to the fracture and amorphisation that occurred during the collapse of the layered structure, as previously observed in other studies.^{44,45} In the aforementioned temperature range, the relative weight loss of NO_2 -LDHs and NO_2 -LDHs@MMT was found to be 23.04% and 21.72%, respectively. The weight loss

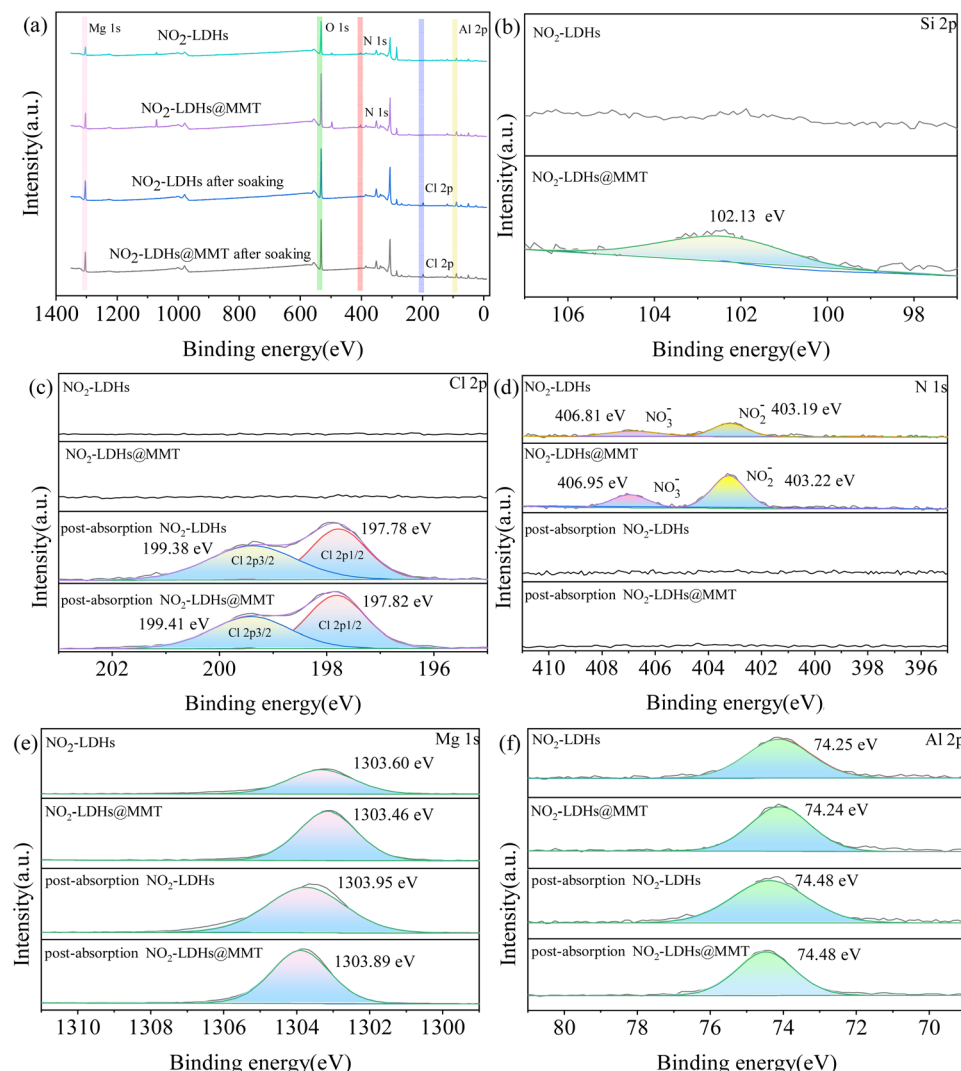


Fig. 7 XPS spectra: (a) survey spectra, (c) Cl 2p, (d) N 1s, (e) Mg 1s, and (f) Al 2p spectra of NO₂-LDHs and NO₂-LDHs@MMT before and after adsorption of chlorine ions in simulated concrete pore solutions, and (b) Si 2p spectra of NO₂-LDHs and NO₂-LDHs@MMT.

rate of NO₂-LDHs was higher than that of NO₂-LDHs@MMT, which can be attributed to the presence of a greater number of hydroxyl groups between the layers. The second stage occurred

between 200 °C and 500 °C and was characterised by the elimination of interlayer water and hydroxyl groups from the layers, as well as the decomposition of nitrate in the interlayer

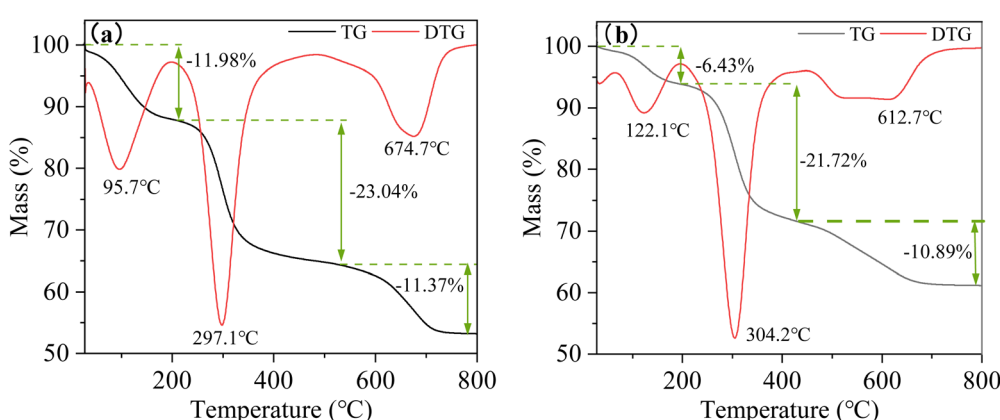


Fig. 8 TG-DTG patterns of the synthesized NO₂-LDHs (a) and NO₂-LDHs@MMT (b).

into nitrite. The layer structure of the LDHs began to collapse. Nevertheless, the restoration of the distinctive layer structure was observed when the material was reintroduced to a solution containing an anion. The third stage spanned the temperature range from 500 °C to 800 °C. This stage saw the removal of the majority of the water, the full dissociation of the interlayer anions, and the degradation of the hydroxyl groups in a disordered manner. This resulted in the formation of magnesium aluminium metal oxides and spinels. This indicates that the layered structure of the hydrotalcite material has been completely and irreversibly destroyed.

Fig. 9 displays the nitrogen adsorption–desorption isotherms and the corresponding Barrett–Joyner–Halenda (BJH) pore size distributions of MMT, NO₂-LDHs and NO₂-LDHs@MMT. In accordance with the classification system established by the International Union of Pure and Applied Chemistry (IUPAC), the adsorption isotherms of all three materials exhibited type IV adsorption behaviour.⁴⁶ The specific surface areas, total pore volumes, and pore sizes of all the synthesised NO₂-LDHs are presented in Table 2. The specific surface areas, as calculated by the BET model, were 46.01, 77.98, and 84.75 m² g⁻¹, respectively, and the total pore volumes were 0.083, 0.224, and 0.284 cm³ g⁻¹, correspondingly belonging to MMT, NO₂-LDHs and NO₂-LDHs@MMT. The specific surface area and total pore volume of NO₂-LDHs@MMT were higher than those of MMT and NO₂-LDHs. The addition of MMT resulted in the formation of a greater number of mesopores in the NO₂-LDHs@MMT. The larger surface area provided

Table 2 Pore texture parameters for the synthesized LDH samples intercalated with NO₂⁻^a

Samples	S_{BET} (m ² g ⁻¹)	V_{total} (cm ³ g ⁻¹)	D_v (nm)
MMT	46.01	0.083	7.19
NO ₂ -LDHs	77.98	0.224	11.49
NO ₂ -LDHs@MMT	84.75	0.284	13.39

^a S_{BET} represents BET specific surface area; V_{total} represents total pore volume; D_v represents average pore diameter.

a greater number of active sites, thereby enhancing the interaction between the adsorbent and the chloride ions. Moreover, the pore size distribution of the three materials indicated that their pore structure was predominantly mesoporous, with an average pore size of 7.19, 11.49, and 13.39 nm, respectively (see Table 2).

The data demonstrated that the pore characteristics of the three distinct layered double hydroxide materials had been examined through nitrogen adsorption–desorption experiments. All three materials, namely MMT, NO₂-LDHs and NO₂-LDHs@MMT, exhibited type IV adsorption behaviour, characterised by a distinct adsorption hysteresis loop, which was typically classified as a type H3 hysteresis loop. This behaviour was typically associated with materials displaying mesoporous range pores. The specific surface area and total pore volume data indicated that NO₂-LDHs@MMT exhibited a higher porosity, which may be attributed to the high specific surface

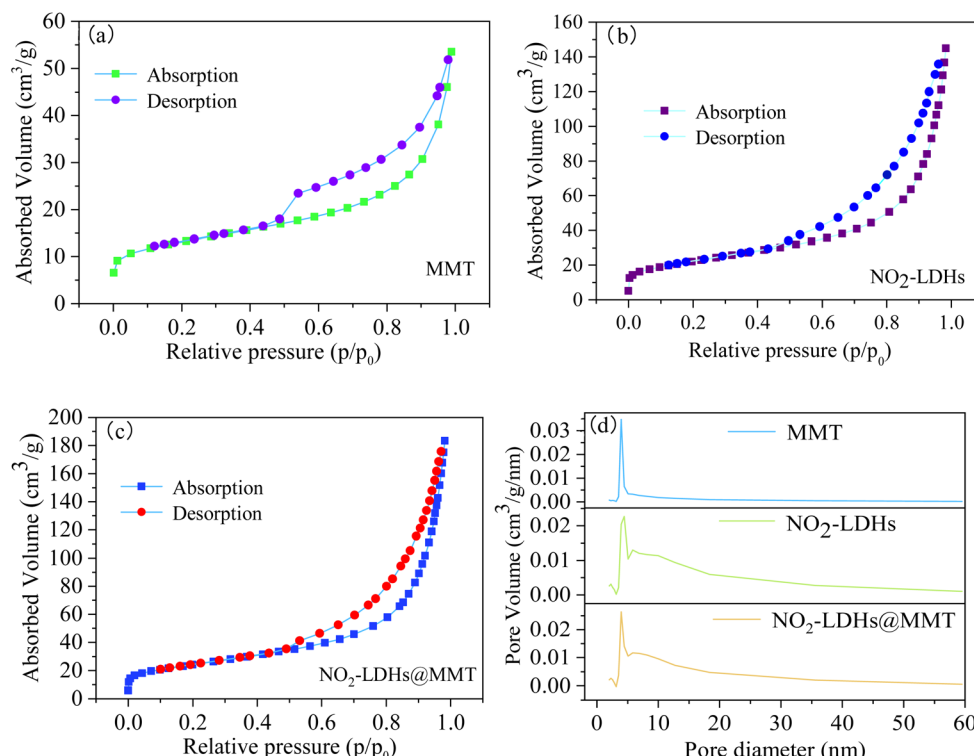


Fig. 9 N₂ adsorption–desorption isotherms and BJH pore size distribution curves of the samples: (a) MMT, (b) NO₂-LDHs, (c) NO₂-LDHs@MMT and (d) pore size distribution curves of samples.



area of MMT, which increased the surface area of LDHs and promoted the formation of mesopores. The high surface area of $\text{NO}_2\text{-LDHs@MMT}$ provided a greater number of active sites for the adsorption of chloride ions, which may have enhanced its adsorption capacity for chlorine ions.^{47,48} The pore size distribution of $\text{NO}_2\text{-LDHs@MMT}$ indicated that it had both micro-pores and mesopores, which may have been beneficial for the adsorption or reaction of molecules of different sizes.^{49,50}

3.3. Adsorption and desorption behaviour of chloride in $\text{NO}_2\text{-LDHs}$ and $\text{NO}_2\text{-LDHs@MMT}$

Fig. 10 illustrates the isotherm adsorption curves of $\text{NO}_2\text{-LDHs}$ and $\text{NO}_2\text{-LDHs@MMT}$ for chloride ions. The data were fitted using the Langmuir (eqn (2)) and Freundlich (eqn (3)) isotherm adsorption models, and the results are presented in Table 3.^{51,52} Considering that the mass of $\text{NO}_2\text{-LDHs}$ or $\text{NO}_2\text{-LDHs@MMT}$ added to simulated concrete pore solutions was 1 g, the effect on the ratio of each ion of the solution was minimal and negligible.

$$Q_e = \frac{W_s K_L C_e}{1 + K_L C_e} \quad (2)$$

$$Q_e = K_F C_e^{1/n} \quad (3)$$

In the low concentration region, the amount of chloride ion binding by $\text{NO}_2\text{-LDHs}$ increased rapidly, reaching a maximum, and then the increase in chloride ion binding capacity slowed down. In particular, when the equilibrium concentration of Cl^- in the system was lower than 200 mmol L⁻¹, the equilibrium load of the two samples increased rapidly with the increase of

the equilibrium concentration of Cl^- . However, when the equilibrium concentration of chloride ions in the solution exceeded 200 mmol L⁻¹, the increase in the equilibrium load of chloride ions by $\text{NO}_2\text{-LDHs}$ decelerated markedly. In contrast, the $\text{NO}_2\text{-LDHs@MMT}$ still demonstrated a notable increase in the equilibrium load of Cl^- at the concentration, indicating that the $\text{NO}_2\text{-LDHs@MMT}$ had exhibited enhanced Cl^- adsorption capacity. The isotherm adsorption curves demonstrated that the correlation coefficient (R^2) of the Langmuir isotherm for $\text{NO}_2\text{-LDHs}$ was 0.9827, while the correlation coefficient (R^2) of the Freundlich isotherm was 0.8606. The correlation coefficient (R^2) of the Langmuir isotherm for $\text{NO}_2\text{-LDHs@MMT}$ was 0.9866, with the correlation coefficient (R^2) of the Freundlich isotherm being 0.9502. The Langmuir isotherm model provided a superior fit to the adsorption capacity data for both samples, indicating that the adsorption of chloride ions by both $\text{NO}_2\text{-LDHs}$ and $\text{NO}_2\text{-LDHs@MMT}$ was a single-layer chemical adsorption process, with all adsorption sites exhibiting equivalent behaviour. This phenomenon can be attributed to the distinctive properties of LDHs, whereby the positive charge remains in the primary layer, resulting in the adsorption of anions to the intermediate layer to maintain electrical neutrality. Therefore, it can be concluded that only a single chloride ion could be fixed at each adsorption site, which was indicative of adsorption occurring on a homogeneous surface. As illustrated in the table, the theoretical maximum adsorption capacity (Q_m) of $\text{NO}_2\text{-LDHs@MMT}$ was 5.181 mmol g⁻¹ (183.93 mg), while that of $\text{NO}_2\text{-LDHs}$ was 2.67 mmol g⁻¹ (94.79 mg). The maximum adsorption capacity of $\text{NO}_2\text{-LDHs@MMT}$ was approximately twice that of $\text{NO}_2\text{-LDHs}$, and the process of adsorbing and consolidating chloride ions was observed to be more effective. Furthermore, the composite structure of $\text{NO}_2\text{-LDHs@MMT}$ also

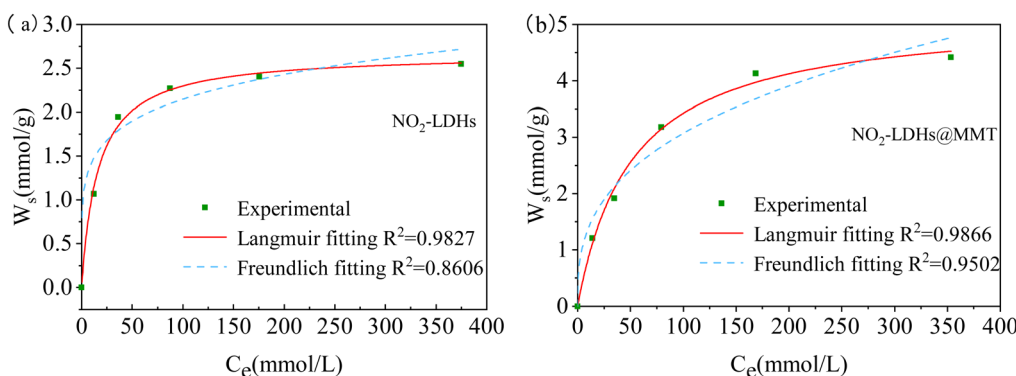


Fig. 10 (a) $\text{NO}_2\text{-LDHs}$ and (b) $\text{NO}_2\text{-LDHs@MMT}$ isotherm adsorption curves of chloride ions in simulated concrete pore solutions.

Table 3 Parameters of the isotherms for the binding of chloride ions in simulated concrete pore solutions for (a) $\text{NO}_2\text{-LDHs}$ and (b) $\text{NO}_2\text{-LDHs@MMT}$, fitted to the Langmuir and Freundlich models

Types	Langmuir			Freundlich		
	K_L (L mmol ⁻¹)	W_s (mmol g ⁻¹)	R^2	$1/n$	K_F	R^2
$\text{NO}_2\text{-LDHs}$	0.062	2.670	0.9827	0.178	0.947	0.8606
$\text{NO}_2\text{-LDHs@MMT}$	0.019	5.181	0.9866	0.349	0.616	0.9502



enhanced its dispersion in solution and adsorption capacity for chloride ions. The SEM image of NO_2 -LDHs@MMT exhibited a core-shell composite structure, which enhanced the dispersibility in solution and the adsorption capacity for chloride ions. The *d*-value of NO_2 -LDHs@MMT in the XRD spectrum was greater than that of NO_2 -LDHs, and the layer spacing was larger, resulting in a reduction in the resistance to the exchange of Cl^- with NO_3^- and NO_2^- . The SEM images and XRD patterns served to corroborate the conclusions drawn from the Cl^- isotherm adsorption curve. It was evident that NO_2 -LDHs@MMT exhibited a superior adsorption capacity, which may be attributed to the fact that MMT enhanced the specific surface area of NO_2 -LDHs and increased the number of active adsorption sites.^{43,44}

3.4. Adsorption and desorption behaviour of chloride in NO_2 -LDHs and NO_2 -LDHs@MMT

Fig. 11 illustrates the alteration in corrosion potential (E_{corr}) of steel samples submerged in simulated concrete pore solutions for the control group, NO_2 -LDHs and NO_2 -LDHs@MMT. It is generally accepted that a corrosion potential (E_{corr}) of less than -350 mV relative to the standard hydrogen electrode (SCE) indicates that the steel is undergoing corrosion.⁴⁸ It was observed that the initial potential of all steel samples was approximately -210 mV (vs. SCE).⁵³ The potential of all samples exhibited a rapid decline during the initial immersion period, followed by a stabilisation trend with the extension of immersion time. It is worthy of note that the blank steel sample exhibited a markedly more rapid decline in E_{corr} than the samples containing NO_2 -LDHs and NO_2 -LDHs@MMT during the initial 10 h of immersion. The presence of NO_2 -LDHs and NO_2 -LDHs@MMT was demonstrated. The equilibrium state was reached, and thus the E_{corr} value of the sample was corrected, indicating that the corrosion potential was low. Further observations revealed that the potential of the NO_2 -LDHs@MMT sample was corrected to that of the NO_2 -LDH sample within the same immersion time. The corrosion potential of the steel was further diminished by the exceptional

inhibition performance of the steel, which was referred to as NO_2 -LDHs@MMT. This phenomenon may be attributed to the larger specific surface area of NO_2 -LDHs@MMT, which has the capacity to adsorb a greater number of chloride ions and release a greater quantity of inhibitory NO_2^- through anion exchange, thereby effectively reducing the corrosion potential of steel.⁵⁴

The Nyquist and Bode plots of the EIS for Q235 samples, which had been passivated in a saturated $\text{Ca}(\text{OH})_2$ solution for seven days and subsequently immersed in *s* simulated concrete pore solutions and containing 1 g L^{-1} of either NO_2 -LDHs or NO_2 -LDHs@MMT for 72 h, are presented in Fig. 12. The impedance values initially manifest resistance behaviour at high frequencies and subsequently exhibit capacitance behaviour at low frequencies, which was consistent with the description provided in the literature.^{20,40} For the same group of samples, the diameter of the curve in the Nyquist diagram exhibited a gradual decrease over time, and the impedance modulus at 0.01 Hz in the Bode diagram also demonstrated a decline, indicating that the corrosion of the steel bar was intensifying. However, the Nyquist plot of the samples containing NO_2 -LDHs or NO_2 -LDHs@MMT exhibited a significantly larger diameter than that of the blank sample at the same immersion time, with the sample containing NO_2 -LDHs@MMT displaying the largest diameter. These findings indicated that the steel bars with NO_2 -LDHs@MMT exhibit enhanced oxide barrier properties and superior corrosion resistance.

To gain further insight into these data, we employed the equivalent circuit model illustrated in Fig. 13 to fit the experimental data. In order to integrate the findings of the literature review with the analysis of the impedance data, the ZSimpWin software was employed to fit the equivalent circuit diagram with $R_s(Q_f(R_f(Q_{\text{dl}}R_{\text{ct}})))$, which has the same response as the electrochemical impedance spectrum measured by the corrosion system. The fitting process provides detailed parameters for each circuit element, which offer valuable insight into the mechanism of action of the corrosion inhibitor. The parameters are presented in Table 4. R_s represents the solution resistance, Q_f and R_f represent the capacitance and resistance of the passive film or corrosion product film, R_{ct} represents the charge transfer resistance, and Q_{dl} represents the double layer capacitance at the steel/solution interface. In consideration of the inhomogeneity of the electrode surface, roughness, porosity, and the inhomogeneity of the current and potential distribution related to the electrode geometry, the Q_f and Q_{dl} were represented in the equivalent circuit by a constant phase element (CPE). The impedance of the CPE was calculated in accordance with eqn (4).

$$Z_{\text{CPE}} = \frac{1}{Q(j\omega)^n} \quad (4)$$

where Q represents the double electric layer capacitance, ω is the angular frequency, j denotes the imaginary number, and n is a dimensionless index that reflects the resemblance between the ideal capacitance and the constant phase angle element (CPE), a characteristic influenced by the electrode's surface roughness and uniformity. When n equaled 1, the CPE functioned in accordance with the characteristics of an ideal

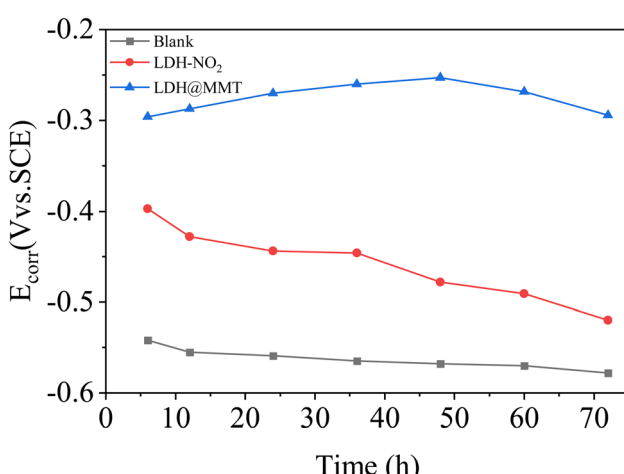


Fig. 11 Change in the corrosion potential (E_{corr}) of steel samples in different corrosion solutions over 72 h.



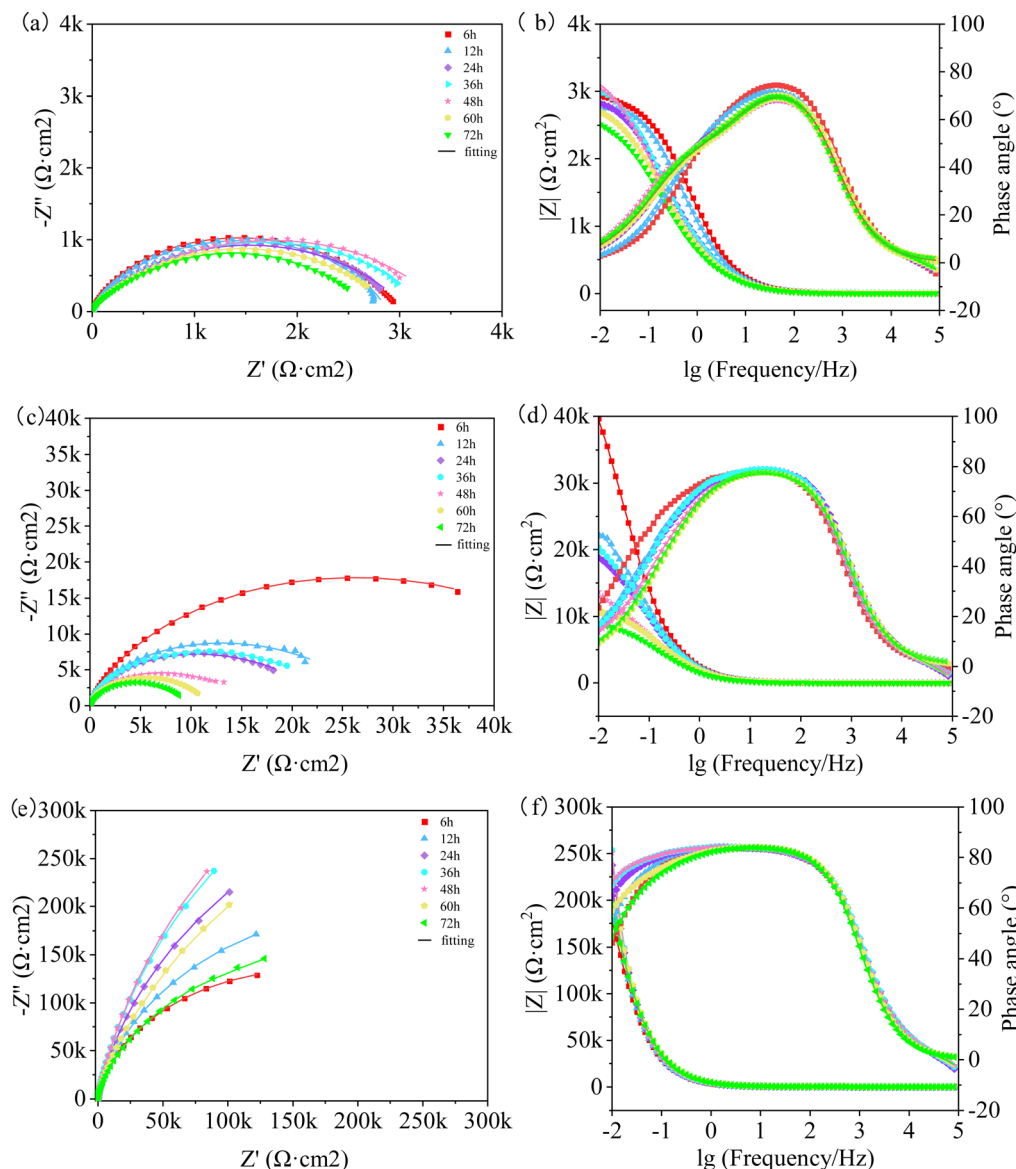


Fig. 12 Nyquist and Bode plots of Q235 steel samples in simulated concrete pore solutions with addition of blank (a, b), NO_2 -LDHs (c, d) and NO_2 -LDHs@MMT (e, f) during 72 h.

capacitor. For values of n between 0.5 and 1, the CPE exhibited behaviour that was not consistent with that of an ideal capacitor. Furthermore, when n equaled zero, the CPE functioned as an ideal resistor.

As illustrated in Fig. 12, the Nyquist plot reveals that the semicircular arcs exhibited by the curves of the samples were relatively complete. The diameter of the capacitive response arc may be employed as an indicator of the charge transfer

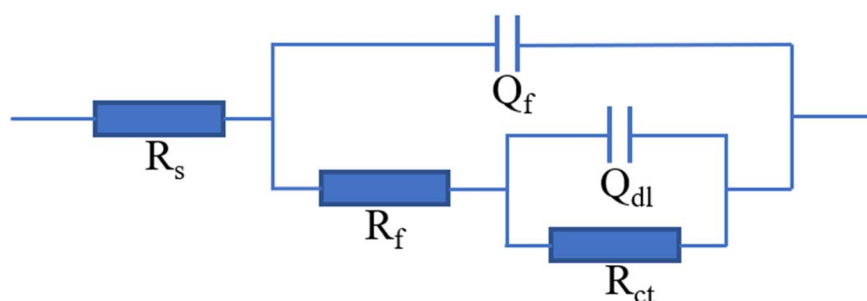


Fig. 13 The equivalent circuit for analyzing EIS data.



Table 4 The fitting parameters obtained from EIS with different immersion times in simulated concrete pore solutions

Sample	Immersion time (h)	R_s (Ωcm^2)	Q_f ($\Omega^{-1} \text{cm}^{-2} \text{s}^n$)	n_f	R_f (Ωcm^2)	Q_{dl} ($\Omega^{-1} \text{cm}^{-2} \text{s}^n$)	n_{dl}	R_{ct} (Ωcm^2)
Blank	6	4.306	8.848×10^5	0.9031	1050	0.0001817	0.5865	1967
	12	4.749	0.0001111	0.8834	909	0.0001898	0.6467	1989
	24	4.528	0.0001281	0.8740	471.7	0.0002783	0.6099	2620
	36	4.582	0.0001222	0.8767	542.5	0.0003287	0.6225	2770
	48	4.392	0.0001442	0.8602	569	0.0003911	0.6282	2891
	60	4.435	0.0001476	0.8573	483.4	0.0003971	0.6255	2469
	72	4.284	0.0001663	0.8415	448.9	0.0004125	0.6132	2293
$\text{NO}_2\text{-LDHs}$	6	6.897	6.706×10^5	0.9126	7500	4.59×10^5	0.5727	4.844×10^4
	12	5.338	7.162×10^5	0.9143	5972	6.278×10^5	0.4813	2.489×10^4
	24	4.68	7.57×10^5	0.9141	5161	6.364×10^5	0.4512	2.178×10^4
	36	4.734	7.717×10^5	0.9124	3566	7.976×10^5	0.4692	2.065×10^4
	48	4.456	9.118×10^5	0.9063	3491	0.0001138	0.4478	1.351×10^4
	60	4.672	0.0001066	0.8957	3374	0.0002091	0.4369	1.152×10^4
	72	4.384	0.0001875	0.8933	3012	0.0002841	0.4236	9814
$\text{NO}_2\text{-LDHs@MMT}$	6	4.607	4.918×10^5	0.9326	2.202×10^5	5.347×10^5	0.7718	9.719×10^4
	12	4.512	4.829×10^5	0.933	2.946×10^5	4.513×10^5	0.9564	1.474×10^5
	24	4.561	4.752×10^5	0.9332	3.986×10^5	1.703×10^5	0.9076	3.75×10^5
	36	4.53	4.682×10^5	0.9346	4.782×10^5	1.317×10^5	0.9599	5.624×10^5
	48	4.728	4.742×10^5	0.9333	5.068×10^5	1.32×10^5	0.9692	6.185×10^5
	60	4.648	4.833×10^5	0.9225	3.813×10^5	1.399×10^5	0.9426	3.845×10^5
	72	4.521	5.172×10^5	0.9212	2.546×10^5	2.088×10^5	0.9389	2.204×10^5

resistance of the sample. Over time, the diameter of the capacitive loop demonstrates a downward trend, indicating that the aggressive chloride ions were gradually causing corrosion of the steel samples. Qualitative indications of the corrosion rate can be obtained from the Nyquist plot in the electrochemical impedance spectrum and the phase angle in the Bode plot. A larger radius in the Nyquist plot is indicative of a greater polarization resistance, which suggests the presence of an effective corrosion inhibitor. A larger phase angle in the Bode plot is indicative of a reduced corrosion rate in the steel. The impedance modulus $|Z|$ in the high-frequency region is primarily indicative of the electrolyte resistance and electrode surface capacitance characteristics, whereas the impedance modulus in the low-frequency region is reflective of the charge transfer and diffusion processes. A higher low-frequency impedance modulus indicates that the penetration of ions and the corrosion process were more impeded, thereby indicating that the corrosion inhibitor exerts a more robust protective effect on the metal.^{55,56}

A further analysis of the Nyquist and Bode plots in Fig. 12 reveals that the Nyquist results for the blank and $\text{NO}_2\text{-LDHs}$ exhibit a similar trend, namely a decrease in the radius of the capacitive arc with increasing immersion time in the solution. The data indicated that chloride ions alter the surface of Q235 steel bars, thereby facilitating corrosion of the steel bars. However, when the steel was immersed in a solution containing 1 g L^{-1} $\text{NO}_2\text{-LDHs}$, the radius of the capacitive arc was found to be one order of magnitude higher than that of the blank sample, indicating that $\text{NO}_2\text{-LDHs}$ had a significant inhibitory effect on the corrosion of Q235 steel. However, the capacitive arc radius continued to decrease at a rapid rate. Furthermore, the Bode plot of the impedance spectrum revealed an initial increase in frequency-impedance modulus, which was followed

by a subsequent decline. It is worthy of note that following immersion of the steel bar in the blank solution for 24 h, the low-frequency impedance modulus $|Z|$ in the low-frequency region of the Bode plot exhibited a higher value than that observed at 6 and 12 h. It was postulated that corrosion products generated by steel bar corrosion may adhere to the electrode surface, potentially impeding ion penetration and charge transfer within a relatively short timeframe. In contrast, the Nyquist and Bode plots of the Q235 steel sample immersed in a 1 g L^{-1} $\text{NO}_2\text{-LDHs@MMT}$ solution exhibit a divergent trend. As the radius of the capacitive arc increases with immersion time, the total impedance and the maximum phase angle in the low frequency range continue to increase until 60 h, when they begin to decrease slowly. The expansion of the capacitive arc's radius signifies an augmentation in the charge transfer resistance, which can be attributed to the incremental release of the rust-inhibiting anions in the $\text{NO}_2\text{-LDHs@MMT}$ and the formation of a protective layer on the metal surface, effectively impeding the corrosion process. The data are presented in Table 4, which demonstrated that the addition of $\text{NO}_2\text{-LDHs}$ and $\text{NO}_2\text{-LDHs@MMT}$ markedly enhances the charge transfer resistance R_{ct} and film resistance R_f of the sample. It was noteworthy that the increase in $\text{NO}_2\text{-LDHs@MMT}$ was particularly pronounced, exhibiting a two-order-of-magnitude enhancement.

The corrosion inhibition efficiency η (%) of the corrosion inhibitor can be calculated using eqn (5).⁵⁷

$$\eta = \frac{R_{ct} - R_{ct}^0}{R_{ct}} \times 100\% \quad (5)$$

where η is the corrosion inhibition efficiency, expressed as a percentage, R_{ct} is the charge transfer resistance after the addition of the corrosion inhibitor and R_{ct}^0 is the charge transfer



resistance of the blank sample (without the corrosion inhibitor).

Following a period of immersion in simulated concrete pore solutions, the corrosion inhibition efficiency of NO_2 -LDHs was determined to be 78.6%, while NO_2 -LDHs@MMT exhibited a significantly higher efficiency of 99.4%. Subsequent to an extended immersion period of 72 h, the corrosion inhibition efficiency of NO_2 -LDHs decreased to 76.63%, while NO_2 -LDHs@MMT demonstrated a consistent and notable inhibition efficiency of 98.9%. The data provide further confirmation of the excellent performance of NO_2 -LDHs@MMT in the inhibition of corrosion. It is possible that the addition of MMT results in an enhancement of the composition and morphology of the mesopores present in the LDHs, thereby increasing the surface area and providing a greater number of active sites. This would result in a more effective release of NO_2^- and Cl^- adsorption. The Q235 steel sample doped with NO_2 -LDHs@MMT demonstrated a notable corrosion inhibition effect throughout the immersion period. The prolongation of the soaking period resulted in the gradual release of anions that inhibit corrosion, thereby enhancing the efficacy of the corrosion inhibition process. The expansion of the capacitive radius in the Nyquist plot and the sustained growth of the total impedance and phase angle in the low-frequency region of the Bode plot provide evidence that NO_2 -LDHs@MMT was an effective corrosion inhibitor, forming a robust and effective protective film. The mechanism demonstrated that NO_2 -LDHs@MMT has considerable potential for practical applications and can effectively protect metal materials from corrosion.

As illustrated in Fig. 14, the Tafel curve enables the observation of significant and irreversible electrochemical reactions occurring on the electrode surface. This was achieved through precise control of the electrode scanning over a wide potential range, allowing for the accurate observation of the electrochemical behaviour of the electrode under test. To ensure the consistency and reliability of the test, the potentiodynamic

polarization test was conducted immediately following the final alternating current (AC) impedance test, thus eliminating the potential for interference with the test sequence. A comparison of the polarization curves of the blank group, NO_2 -LDHs and NO_2 -LDHs@MMT reveals a notable shift in the corrosion potential (E_{corr}) in a positive direction. In particular, the corrosion potential of Q235 steel in the blank solution was -0.682 V, whereas the corrosion potential increased to -0.613 and -0.479 V, respectively. The considerable enhancement in potential demonstrates that NO_2 -LDHs and NO_2 -LDHs@MMT have markedly elevated electrochemical stability, which has led to a notable reduction in corrosion tendency. Moreover, the Tafel extrapolation method was employed to accurately extract pivotal parameters from the polarization curves, including the corrosion potential (E_{corr}), corrosion current density (i_{corr}), and the Tafel slopes of the anode and cathode (β_a and β_c) (see Table 5). It was noteworthy that the sample treated with NO_2 -LDHs@MMT exhibited the lowest corrosion current density (2.212×10^{-6} A cm^{-2}) and the most positive corrosion potential (-0.479 V). This was further confirmed by the key parameters extracted by Tafel extrapolation, emphasising the excellent performance of NO_2 -LDHs@MMT in inhibiting corrosion, which may be attributed to its unique chemical structure and surface properties that effectively isolate the corrosive medium from direct contact with the metal substrate, thereby slowing down the corrosion process.

The corrosion inhibition efficiency (η_i) of the inhibitor could be calculated from the corrosion current (i_{corr}) using eqn (6).⁵⁷

$$\eta = \frac{i_{\text{corr}}^0 - i_{\text{corr}}}{i_{\text{corr}}^0} \times 100\% \quad (6)$$

where η is the corrosion inhibition efficiency, expressed as a percentage and i_{corr} is the corrosion current after the corrosion inhibitor has been added. The corrosion inhibition efficiency (η) was calculated using the corrosion current density, and the results demonstrated that the corrosion inhibition efficiency of NO_2 -LDHs@MMT was as high as 90.60%, which was markedly superior to that of NO_2 -LDHs, which also exhibited a discernible corrosion inhibition effect, albeit relatively weak.

In light of the findings of the potentiodynamic polarization test and EIS, the following scientific conclusions may be drawn. The NO_2 -LDHs@MMT composites provide long-term and highly effective protection for Q235 steel bars in chloride ion environments. The excellent corrosion inhibition performance can be attributed to the following factors: firstly, the distinctive core-shell daisy-like composite configuration of NO_2 -LDHs@MMT markedly enhances the specific surface area of the material, facilitating the creation of a greater number of active sites for the adsorption of chloride ions. Secondly, the anion exchange process enables the release of the inhibitory NO_2^- ions, effectively slowing down the corrosion rate of the steel bars. Ultimately, the formation of a robust and compact protective layer on the steel bars impedes the penetration of the corrosive medium and the charge transfer process. It can thus be concluded that NO_2 -LDHs@MMT has considerable potential for application in the field of metal corrosion protection.

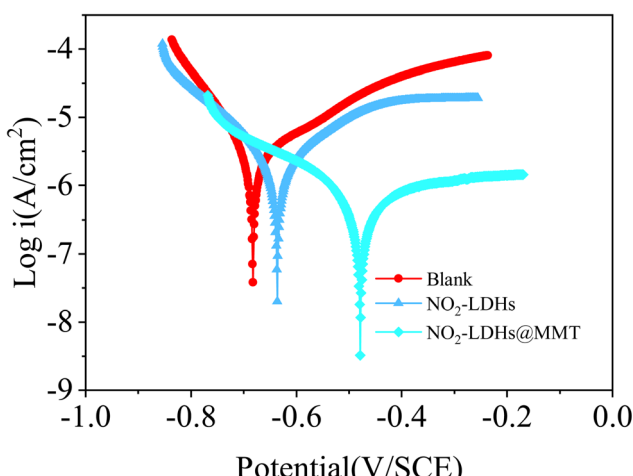


Fig. 14 Tafel curve of carbon steels in simulated concrete pore solutions with addition of NO_2 -LDHs@MMT, NO_2 -LDHs and blank (after soaking in simulated concrete pore solutions and with addition of NO_2 -LDHs@MMT, NO_2 -LDHs and blank for 72 h).



Table 5 The electrochemical parameters fitted by Tafel curves

Samples	E_{corr} (V)	i_{corr} (A cm $^{-2}$)	$-\beta_c$ (V dec $^{-1}$)	β_a (V dec $^{-1}$)	η (%)
Blank	-0.68	7.623×10^6	7.21	5.44	—
NO ₂ -LDHs	-0.61	2.352×10^6	7.11	5.16	69.14
NO ₂ -LDHs@MMT	-0.48	7.112×10^7	4.63	3.73	90.60

The objective of this experiment is to further test the actual corrosion protection effect of NO₂-LDHs or NO₂-LDHs@MMT on steel bars. The full and high-resolution XPS spectra of the Q235 rebar surface were surveyed after seven days of passivation in a saturated Ca(OH)₂ solution or a saturated Ca(OH)₂ solution containing 1 g L⁻¹ NO₂-LDHs or NO₂-LDHs@MMT, as illustrated in Fig. 15. From the Fe 2p high-resolution spectra (Fig. 15c, e and g), it is evident that the passive film on the steel surface contains Fe²⁺ ions, primarily existing in the form of FeO, which serves as a major component of the passivation layer responsible for inhibiting corrosion. In addition to the Fe²⁺ peak, several satellite peaks (FeO-sat) were also recorded. Furthermore, the steel surface curve reveals the presence of metallic Fe (Fe⁰).⁵⁸ The O 1s spectra (Fig. 15d, f and h) indicate two states in the steel's passive film: O²⁻ and OH⁻, attributed to iron oxides and hydroxides, respectively.⁵⁹

In both the blank group (Fig. 15c) and the group containing only NO₂-LDHs (Fig. 15e), the XPS spectra show not only Fe₂O₃ but also a partial signal for Fe⁰, suggesting that the passive film is not entirely dense and that portions of the metallic substrate remain exposed. The presence of Fe₂O₃ indicates localized oxidation, while the Fe⁰ signal implies that the oxide layer has not formed a complete protective barrier, leaving the material susceptible to further corrosion.⁶⁰ In contrast, for the 1 g L⁻¹ NO₂-LDHs@MMT group (Fig. 15g), the XPS analysis reveals a significant increase in the Fe²⁺ and O²⁻ ratio, while the Fe⁰ peak is markedly weakened or nearly absent, suggesting the formation of a more stable and compact oxide or hydroxide layer on the steel surface.

As demonstrated by the O 1s XPS split-peak fitting (Fig. 15d, f and h), the NO₂-LDHs@MMT group exhibited 24.3% O²⁻ occupancy, which is 3% and 11% higher O²⁻ occupancy than that of the NO₂-LDH group and the blank group, respectively, and which is a good indication that the NO₂-LDHs@MMT group formed the most dense iron oxide passivation layer. According to Fig. 15b, the relative content of iron oxides in the NO₂-LDHs@MMT-treated rebar reaches 100% (including satellite peaks), which is 8.5% higher than that in the NO₂-LDH group and 13.2% higher than that in the blank group. Combined with the high charge-transfer resistance (R_{ct}) and a more pronounced impedance modulus from the EIS measurements, these results confirm that NO₂-LDHs@MMT provides enhanced corrosion protection *via* a dual mechanism. On one hand, the sustained release of NO₂⁻ promotes the formation of protective oxide layers; on the other, the core–shell structure of MMT and LDHs effectively adsorbs Cl⁻ and prevents corrosive ions from reaching the steel substrate. This synergy significantly reduces the corrosion rate and improves the integrity of the passive film,

making the NO₂-LDHs@MMT group exhibit the most favorable anti-corrosion performance.

3.5. Proposed mechanism

The synthesis of NO₂-LDHs and NO₂-LDHs@MMT composites was conducted using the *in situ* growth-template method. The pH value plays a pivotal role in determining the properties of NO₂-LDHs@MMT composites. Under alkaline conditions (pH = 10), the laminates of LDHs were fully formed, while the enhanced negative electronegativity of the MMT surface promoted the deposition and vertical growth of LDHs. Conversely, at lower pH values, the lamellar structure may be unstable, which in turn reduces the adsorption properties of the material. The selection of the precipitation time directly impacts the structure and properties of the composites. A prolonged precipitation time may result in an overgrowth of LDH lamellae on the MMT surface, which in turn increases inter-lamellar stacking and reduces the effective number of active sites.^{61,62} MMT was employed as a template material and complexed with NO₂-LDHs to form a daisy-like core–shell structure. This structure significantly enhances the specific surface area and the number of active sites, thereby providing a new method for the improvement of chloride ion adsorption and rust inhibition performance. This is in marked contrast to the LDH materials with unoptimised substrate structures in existing studies. The NO₂-LDHs@MMT composite material displays an exceptional capacity for chloride ion adsorption and offers robust reinforcement protection in chloride ion environments, largely due to its distinctive biomimetic core–shell daisy-like structure, as shown in the pictures in Fig. 5 and 7. It can be reasonably inferred that the observed effect was attributable to the synergistic interaction between the material's structural properties, composition, and surface chemistry. The high specific surface area and rich pore structure of NO₂-LDHs@MMT, particularly the presence of mesopores, markedly enhances the material's adsorption capacity. The incorporation of MMT not only elevates the specific surface area of NO₂-LDHs (from 77.98 m² g⁻¹ to 84.74 m² g⁻¹), but also stimulates the generation of additional mesopores, thereby furnishing a greater number of active sites for the adsorption of chloride ions. The enhanced specific surface area and porosity of the NO₂-LDHs@MMT facilitate the capture and fixation of chloride ions in chloride-ion environments, thereby reducing the concentration of free chloride ions and consequently decelerating the corrosion rate of steel bars.

The LDHs in the NO₂-LDHs@MMT exhibit a positive charge, which attracts and adsorbs negatively charged chloride ions. Upon entering the LDH layer, chloride ions engage in an anion



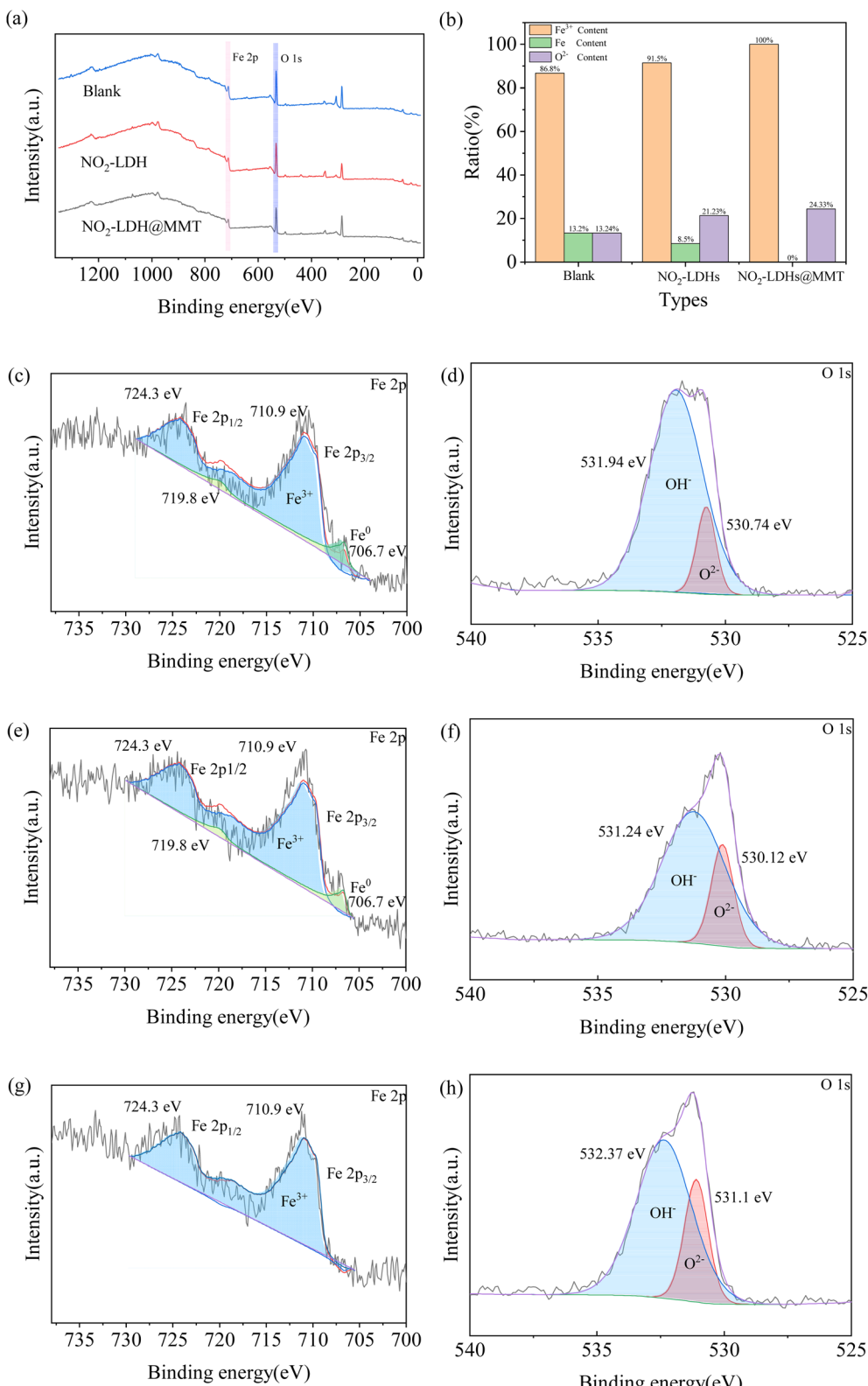


Fig. 15 XPS of rebar electrodes immersed in $\text{Ca}(\text{OH})_2$ passivated for 7 d containing (c and d) blank; (e and f) 1 g L^{-1} NO_2 -LDHs; (g and h) 1 g L^{-1} NO_2 -LDHs@MMT (a) full and high-resolution spectra; (b) Fe^{3+} vs. O^{2-} content calculated from XPS results.

exchange reaction with the preexisting NO_3^- and NO_2^- ions, thereby maintaining the electrical neutrality of the layer. The anion exchange process not only facilitates the effective removal

of chloride ions, but also releases inhibitory NO_2^- ions into the solution. The released NO_2^- ions can form a dense protective film on the surface of the steel bar, preventing direct contact

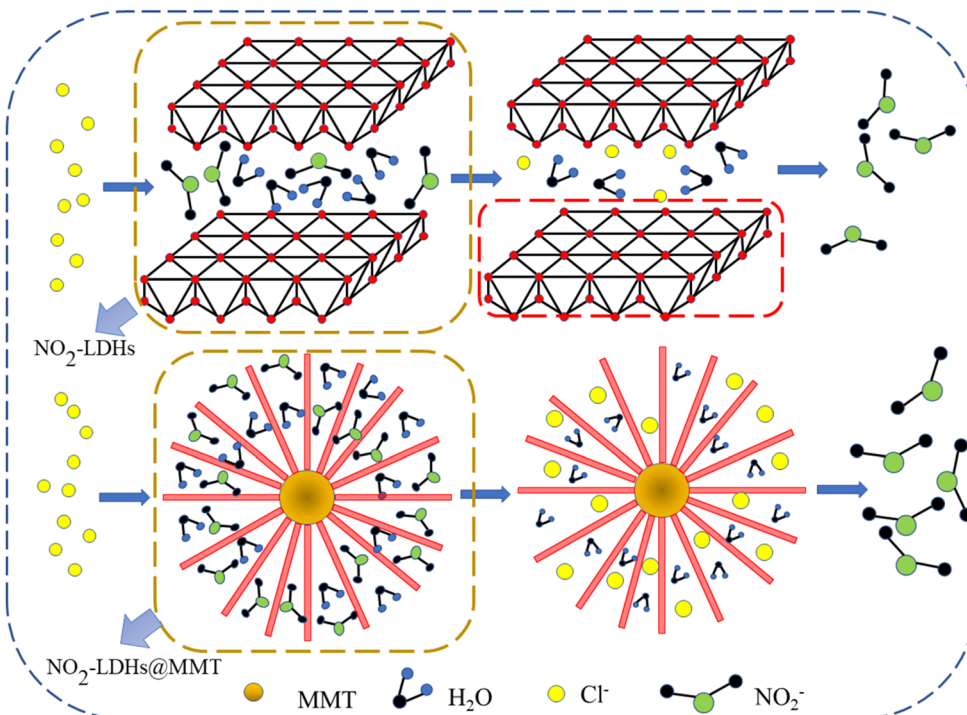


Fig. 16 Schematic diagram of NO_2^- and Cl^- displacement in composite $\text{NO}_2\text{-LDHs@MMT}$.

between the corrosive media, such as chloride ions, and the steel bar, thereby further slowing down the corrosion process of the steel bar, as exhibited in the XPS spectra in Fig. 7. Furthermore, the protective film formed by $\text{NO}_2\text{-LDHs@MMT}$ on the surface of the steel bar is not only dense and stable, but also effectively prevents the penetration of corrosive media and the charge transfer process, as exhibited in the XPS spectra in Fig. 15. The results of EIS and potentiodynamic polarization curve tests demonstrate that the incorporation of $\text{NO}_2\text{-LDHs@MMT}$ markedly enhances the charge transfer resistance and corrosion potential of the steel bar, while concurrently reducing the corrosion current density. These findings substantiate the efficacy of $\text{NO}_2\text{-LDHs@MMT}$ as an effective corrosion inhibitor for steel bars. The stable protective film formed by $\text{NO}_2\text{-LDHs@MMT}$ is pivotal for shielding steel bars from corrosion. The $\text{NO}_2\text{-LDHs@MMT}$ composite exhibits a sustained release of the rust-blocking anion NO_2^- through the directional exchange of interlayer anions, while effectively adsorbing chloride ions. This dynamic function regulation mechanism is more advantageous than the single static adsorption performance of traditional LDH materials, offering a new avenue for the long-term application of composites in complex corrosive environments. In order to gain a more intuitive understanding of the process and mechanism of Cl^- adsorption, the exchange of NO_2^- and Cl^- is illustrated in $\text{NO}_2\text{-LDHs@MMT}$, as shown in Fig. 16. More composite strategies of layered materials with different substrates can be explored in the future to further optimise the dynamic functional modulation ability of the materials.

4. Conclusion

(1) The $\text{NO}_2\text{-LDHs}$ and their core-shell $\text{NO}_2\text{-LDHs@MMT}$ composites were successfully synthesized *via* *in situ* co-precipitation. Structural characterization through SEM-EDS, XRD, and FTIR analyses confirmed the unique chrysanthemum-like morphology of $\text{NO}_2\text{-LDHs@MMT}$, where vertically aligned LDH nanosheets interlocked on MMT surfaces. HRTEM imaging revealed an open hierarchical architecture with minimal nanosheet stacking, attributed to the templating effect of MMT. Nitrogen physisorption analysis demonstrated a 1.8-fold increase in specific surface area ($84.74 \text{ m}^2 \text{ g}^{-1}$ for $\text{NO}_2\text{-LDHs@MMT}$ *vs.* $77.98 \text{ m}^2 \text{ g}^{-1}$ for $\text{NO}_2\text{-LDHs}$) and a 26.8% higher total pore volume ($0.284 \text{ cm}^3 \text{ g}^{-1}$ *vs.* $0.224 \text{ cm}^3 \text{ g}^{-1}$), primarily due to MMT-induced mesopore formation. This enhanced porosity provided abundant active sites for chloride adsorption.

(2) Chloride adsorption studies revealed monolayer chemisorption behavior following the Langmuir isotherm model ($R^2 = 0.9866$). The $\text{NO}_2\text{-LDHs@MMT}$ composite exhibited a maximum adsorption capacity of 183.93 mg g^{-1} ($5.181 \text{ mmol g}^{-1}$), doubling that of pristine $\text{NO}_2\text{-LDHs}$ (94.79 mg g^{-1} , 2.67 mmol g^{-1}). XPS analysis confirmed the anion exchange mechanism: characteristic $\text{Cl} 2p$ peaks (198.6 eV) emerged post-adsorption, accompanied by a 62% reduction in $\text{NO}_2^-/\text{NO}_3^-$ signals, directly evidencing displacement of interlayer anions by Cl^- . This synergistic effect of enhanced surface area and optimized ion exchange capacity underpinned the superior adsorption performance.

(3) The experimental results obtained from the EIS and kinetic potential polarisation curves demonstrate that the

incorporation of NO_2 -LDHs and NO_2 -LDHs@MMT leads to a substantial enhancement in the corrosion resistance of Q235 rebar in chlorinated solutions. The experimental findings demonstrate that, following a 72 h immersion period, the corrosion inhibition efficiency of NO_2 -LDHs@MMT reaches an optimal level of 98.9%, which is considerably higher than that of NO_2 -LDHs, at 76.63%. This phenomenon can be attributed to the sustained release of NO_2^- from NO_2 -LDHs@MMT on the surface of the reinforcement bar, leading to the formation of a stable and effective protective layer. This layer effectively hinders the penetration of the corrosive medium and the charge transfer process. The EIS and polarisation curves substantiated the sustained release mechanism of NO_2 -LDHs@MMT, indicating that it formed a stable protective film on the surface of the reinforcement bar.

(4) With the prolongation of immersion time, the corrosion potentials of all experimental groups decreased, but the corrosion potentials of the NO_2 -LDHs@MMT group decreased at the slowest rate and finally remained at a high level. In addition, the lowest corrosion current density was observed in the NO_2 -LDHs@MMT group, which further proved its excellent protective efficacy for steel reinforcement. These findings indicate that NO_2 -LDHs@MMT can effectively reduce the corrosion tendency and corrosion rate of steel bars.

(5) From the results of FTIR, XRD and XPS analyses, the corrosion protection effect of NO_2 -LDHs@MMT on steel reinforcement is mainly attributed to the double-layer protection mechanism. Firstly, the adsorption of chloride anions reduces the concentration of harmful ions in the solution and reduces the erosion of corrosive media on steel bars. Secondly, NO_2^- released by NO_2 -LDHs@MMT formed a dense protective film on the rebar surface, which further hindered the corrosion process. The XPS test results showed that the FeO content on the surface of the NO_2 -LDHs@MMT-treated rebar was significantly increased, suggesting the formation of a denser, more corrosion-resistant passivation film. This double-layer protection mechanism endows NO_2 -LDHs@MMT with long-term effective protection of steel bars in chloride ion environments, demonstrating its great potential for application in the field of metal corrosion protection.

The manuscript presents a comprehensive investigation into the promotion of MMT on the properties of NO_2 -LDHs@MMT composites. Nevertheless, the precise impact of experimental variables (e.g., pH, temperature, precipitation time) on the structure and characteristics of the composites remains to be fully elucidated and investigated. These conditions may exert a pivotal influence on the specific surface area, crystal structure and the number of adsorption sites of the materials. It is recommended that these factors be subjected to comprehensive investigation through systematic variable experiments in the future.

Data availability

The data that support the findings of this study are available from the corresponding author, Xiaoyi Zhang (xy-zhang@fjtu.edu.cn), upon reasonable request.

Author contributions

Xiaoyi Zhang: conceptualization, supervision, writing – original draft, funding acquisition. Binxin Gan: writing – original draft. Chen Wu: writing – review and editing. Guoliang Lin: methodology, writing – review and editing. Shenglan Ma: supervision, funding acquisition. Yongbin Ye: data curation. Wanxi Jiang: data curation. Wenjin Huang: data curation.

Conflicts of interest

The authors declare that they have no known competing financial interests or personal relationships that could have appeared to influence the work reported in this paper.

Acknowledgements

The authors would like to express their gratitude to the following organisations for their financial support: The Key Research and Development Plan of Fujian Province (No. 2022H6032), Guiding Project of Fujian Provincial Science and Technology Department (No. 2023H0016), Education Foundation of Fujian Province (No. JAT210287), and the Fujian Key Laboratory of Digital Simulations for Coastal Civil Engineering, School of Architecture and Civil Engineering, Xiamen University (No. DSCEOF-2202).

References

- 1 O. Amiri, A. Aït-Mokhtar, P. Dumargue and G. Touchard, *Electrochim. Acta*, 2001, **46**, 1267–1275.
- 2 Z. Dong, Y. Sun, H. Zhu, G. Wu, Z. Yan and F. Lu, *Compos. Struct.*, 2022, **288**, 115392.
- 3 S. Li, H. Lu, X. Huang and J. Yang, *Ocean Eng.*, 2022, **255**, 111404.
- 4 S. A. Mangi, M. H. Wan Ibrahim, N. Jamaluddin, M. F. Arshad and S. Shahidan, *Eng. Sci. Technol. Int. J.*, 2019, **22**, 929–938.
- 5 Z. Yuan, Q. Li and K. Li, *Struct. Saf.*, 2024, **106**, 102405.
- 6 J. Bao, J. Wei, P. Zhang, Z. Zhuang and T. Zhao, *Cem. Concr. Compos.*, 2022, **130**, 104511.
- 7 J. Chen, Y. Song, D. Shan and E.-H. Han, *Corros. Sci.*, 2012, **65**, 268–277.
- 8 R. Gao, D. Yan, D. G. Evans and X. Duan, *Nano Res.*, 2017, **10**, 3606–3617.
- 9 Y. Zhao, H. Lin, M. Chen and D. Yan, *Ind. Eng. Chem. Res.*, 2014, **53**, 3140–3147.
- 10 D. Yan, J. Lu, L. Chen, S. Qin, J. Ma, M. Wei, D. G. Evans and X. Duan, *Chem. Commun.*, 2010, **46**, 5912–5914.
- 11 Y. Chen, Z. Shui, W. Chen and G. Chen, *Constr. Build. Mater.*, 2015, **93**, 1051–1058.
- 12 R. Gao and D. Yan, *Chem. Sci.*, 2017, **8**, 590–599.
- 13 R. Gao, D. Yan and X. Duan, *Cell Rep. Phys. Sci.*, 2021, **2**, 100536.
- 14 M. Zhai, J. Zhao, D. Wang, X. Gao, Q. Wang, Z. Li and M. Zhang, *Nanotechnol. Rev.*, 2022, **11**, 2857–2874.

15 Y. Liu, N. Wang, J. H. Pan, F. Steinbach and J. Caro, *J. Am. Chem. Soc.*, 2014, **136**, 14353–14356.

16 X. H. Zhu, X. J. Kang, K. Yang and C. H. Yang, *Constr. Build. Mater.*, 2017, **132**, 290–295.

17 H. Tatematsu and T. Sasaki, *Cem. Concr. Compos.*, 2003, **25**, 123–129.

18 Z. H. Shui, R. Yu, Y. X. Chen, P. Duan, J. T. Ma and X. P. Wang, *Constr. Build. Mater.*, 2018, **176**, 228–240.

19 J. Xu, J. Wei, G. Ma and Q. Tan, *Corros. Sci.*, 2020, **176**, 108940.

20 J. Xu, Q. Tan and Y. Mei, *Corros. Sci.*, 2020, **163**, 108223.

21 P. Zhou, J. Xu and L. Yu, *Corros. Sci.*, 2022, **195**, 109997.

22 A. E. A. Aboubakr, W. M. A. El Rouby, M. D. Khan, A. A. Farghali and N. Revaprasadu, *Appl. Surf. Sci.*, 2020, **508**, 145100.

23 H. Huang, C. Xia, D. Liang, Y. Xie, F. Kong, J. Fu, Z. Dou, Q. Yang, W. Suo, Q. Zhang and Z. Meng, *Chem. Eng. J.*, 2022, **431**, 134113.

24 F.-D. Zhang, C.-G. Lin, S.-J. Diao, H. N. Miras and Y.-F. Song, *Inorg. Chem. Front.*, 2021, **8**, 1324–1333.

25 K. Ruengkajorn, V. Erastova, J.-C. Buffet, H. C. Greenwell and D. O'Hare, *Chem. Commun.*, 2018, **54**, 4394–4397.

26 S. Mallakpour, M. Hatami and C. M. Hussain, *Adv. Colloid Interface Sci.*, 2020, **283**, 102216.

27 S. Feng, Y. Ma, S. Wang, S. Gao, Q. Huang, H. Zhen, D. Yan, Q. Ling and Z. Lin, *Angew. Chem., Int. Ed.*, 2022, **61**, e202116511.

28 M. A. Mushtaq, M. Ahmad, A. Shaheen, A. Mehmood, G. Yasin, M. Arif, Z. Ali, P. Li, S. N. Hussain, M. Tabish, A. Kumar, S. R. Ajmal, W. Raza, M. Akhtar, A. Saad and D. Yan, *ACS Mater. Lett.*, 2024, 3090–3111.

29 W. He, Y. Yang, L. Wang, J. Yang, X. Xiang, D. Yan and F. Li, *ChemSusChem*, 2015, **8**, 1568–1576.

30 C. Chen, R. Felton, J. C. Buffet and D. O'Hare, *Chem. Commun.*, 2015, **51**, 3462–3465.

31 C. Chen, C. F. H. Byles, J. C. Buffet, N. H. Rees, Y. Wu and D. O'Hare, *Chem. Sci.*, 2016, **7**, 1457–1461.

32 X. Ke, S. A. Bernal and J. L. Provis, *Cem. Concr. Res.*, 2017, **100**, 1–13.

33 R. Li, T. Xue, R. Bingre, Y. Gao, B. Louis and Q. Wang, *ACS Appl. Mater. Interfaces*, 2018, **10**, 34834–34839.

34 P. Zhou, J. Xu and Z. Wang, *Appl. Clay Sci.*, 2023, **240**, 106975.

35 J. Li, T. Wu, E. Zhuang, W. Cao and Z. Chen, *Constr. Build. Mater.*, 2024, **411**, 134779.

36 Q. Zhou, X. Dai, K. Li, C. Zhang, X. Zhang, Z. Du, S. Yi, P. Yang, J. Rao and Y. Zhang, *CrystEngComm*, 2022, **24**, 6546–6557.

37 D. B. Jiang, C. Jing, Y. Yuan, L. Feng, X. Liu, F. Dong, B. Dong and Y. X. Zhang, *J. Colloid Interface Sci.*, 2019, **540**, 398–409.

38 G. Sun, J. Zhang, X. Li, B. Hao, F. Xu and K. Liu, *J. Environ. Chem. Eng.*, 2023, **11**, 110129.

39 Y. Jiang, R. Xu, B. Cai, H. Gu, L. Zhang, X. Yang, H. Shen and G. Liu, *Electrochim. Acta*, 2024, **474**, 143542.

40 J. Sun, B. Liang, Y. Huang and X. Wang, *Catal. Today*, 2016, **274**, 123–128.

41 P. Lakhani and C. K. Modi, *Mol. Catal.*, 2024, **559**, 114080.

42 H. Bahman, K. Gharanjig, E. Ghasemi, H. Kazemian, M. Hosseinezhad and H. Gharanjig, *J. Mol. Struct.*, 2025, **1319**, 139616.

43 J. Zhong, S. Lin and J. Yu, *Desalination*, 2021, **505**, 114983.

44 M. Szabados, Z. Kónya, Á. Kukovecz, P. Sipos and I. Pálinkó, *Appl. Clay Sci.*, 2019, **174**, 138–145.

45 D. Tichit, G. Layrac and C. Gérardin, *Chem. Eng. J.*, 2019, **369**, 302–332.

46 I. Atkinson, E. M. Anghel, L. Predoana, O. C. Mocioiu, L. Jecu, I. Raut, C. Munteanu, D. Culita and M. Zaharescu, *Ceram. Int.*, 2016, **42**, 3033–3045.

47 G. Ma, J. Xu and Z. Wang, *Corros. Sci.*, 2023, **225**, 111571.

48 X. Dai, C. Jing, K. Li, X. Zhang, D. Song, L. Feng, X. Liu, H. Ding, H. Ran, K. Zhu, N. Dai, S. Yi, J. Rao and Y. Zhang, *Appl. Clay Sci.*, 2023, **233**, 106815.

49 M. Liu, T. Wang, H. Ma, Y. Fu, K. Hu and C. Guan, *Sci. Rep.*, 2014, **4**, 7147.

50 F. Chengqian, D. Yimin, C. Ling, W. Zhiheng, L. Qi, L. Yaqi, C. Ling, L. Bo, Z. Yue-Fei, L. Yan and W. Li, *Sep. Purif. Technol.*, 2022, **295**, 121227.

51 I. Langmuir, *J. Am. Chem. Soc.*, 1918, **40**, 1361–1403.

52 N. M. Agyei, C. A. Strydom and J. H. Potgieter, *Cem. Concr. Res.*, 2000, **30**, 823–826.

53 E. Zhuang, J. Li, Z. Chen, B. Yu and Y. Nong, *Composites, Part B*, 2024, **277**, 111414.

54 X. Zhou, H. Yang and F. Wang, *Corros. Sci.*, 2012, **54**, 193–200.

55 D. S. Patil, S. A. Pawar, S. H. Lee and J. C. Shin, *J. Electroanal. Chem.*, 2020, **862**, 114012.

56 P. Li, M. Wang, X. Duan, L. Zheng, X. Cheng, Y. Zhang, Y. Kuang, Y. Li, Q. Ma, Z. Feng, W. Liu and X. Sun, *Nat. Commun.*, 2019, **10**, 1711.

57 F. Zhi, L. Jiang, M. Jin, P. Xu, B. Xiao, Q. Jiang, L. Chen and Y. Gu, *Constr. Build. Mater.*, 2020, **259**, 120425.

58 R. Chen, J. Hu, Y. Ma, W. Guo, H. Huang, J. Wei, S. Yin and Q. Yu, *Corros. Sci.*, 2020, **165**, 108393.

59 L. Freire, M. J. Carmezim, M. G. S. Ferreira and M. F. Montemor, *Electrochim. Acta*, 2010, **55**, 6174–6181.

60 M. Chen, H. Zheng, L. Yu, Y. Cai, Q.-f. Liu, Z. Wang, H. Xie and W. Li, *Chem. Eng. J.*, 2024, **485**, 150164.

61 P. Wang, X. Zhang, B. Zhou, F. Meng, Y. Wang and G. Wen, *J. Environ. Chem. Eng.*, 2023, **11**, 111191.

62 S. Riaz, A. u. Rehman, Z. Akhter, T. Najam, I. Hossain, M. R. Karim, M. A. Assiri, S. S. Ahmad Shah and M. A. Nazir, *Mater. Today Sustain.*, 2024, 100897.

